CORRECTED 7 JANUARY 2022; SEE ERRATUM

SCIENCE ADVANCES | RESEARCH ARTICLE

GEOCHEMISTRY

Heating events in the nascent solar system recorded by rare earth element isotopic fractionation in refractory inclusions

J. Y. Hu[1,2]*, N. Dauphas[1,2], F. L. H. Tissot[1,3], R. Yokochi[2], T. J. Ireland[1,2,4], Z. Zhang[1,2], A. M. Davis[2], F. J. Ciesla[2], L. Grossman[2], B. L. A. Charlier[5], M. Roskosz[6], E. E. Alp[7], M. Y. Hu[7], J. Zhao[7]

Equilibrium condensation of solar gas is often invoked to explain the abundance of refractory elements in planets and meteorites. This is partly motivated, by the observation that the depletions in both the least and most refractory rare earth elements (REEs) in meteoritic group II calcium-aluminum–rich inclusions (CAIs) can be reproduced by thermodynamic models of solar nebula condensation. We measured the isotopic compositions of Ce, Nd, Sm, Eu, Gd, Dy, Er, and Yb in eight CAIs to test this scenario. Contrary to expectation for equilibrium condensation, we find light isotope enrichment for the most refractory REEs and more subdued isotopic variations for the least refractory REEs. This suggests that group II CAIs formed by a two-stage process involving fast evaporation of preexisting materials, followed by near-equilibrium recondensation. The calculated time scales are consistent with heating in events akin to FU Orionis– or EX Lupi–type outbursts of eruptive pre–main-sequence stars.

INTRODUCTION

It is generally accepted that the building blocks of the terrestrial planets and other inner solar system objects experienced vaporization and homogenization at high temperature at the birth of the solar system (*1*). According to this view, solids and perhaps liquids condensed as the nebula cooled from gas of solar composition [e.g., (*2*, *3*)]. The composition of the condensates evolved during cooling following a sequence, from more refractory phases rich in Ca, Al, and Ti to more volatile phases rich in K and Na. The condensation sequence is hinted at by the mineralogical and chemical compositions of partial condensed relicts known as refractory inclusions [or Ca-, Al-rich inclusions (CAIs)] that were isolated from the remaining nebular gas before major rock-forming elements such as Si, Mg, and Fe were fully condensed. This early isolation led refractory inclusions to preserve large enrichments in refractory elements such as the rare earth elements (REEs) and distinctively fractionated chemical abundance patterns. A readily identifiable fractionated REE pattern in CAIs is known as group II (*4*, *5*), which is present in 40% of all CAIs, most notably those of fine-grained texture [70% of all CAIs have nonchondritic relative abundances of the REEs; (*6*)]. Group II CAIs have so far only been documented in carbonaceous chondrites, but this could be due to the scarcity of CAIs in noncarbonaceous chondrites. Group II REE patterns are marked by depletions in the least refractory (Eu and Yb) and most refractory REEs (Gd-Er and Lu), while REEs of intermediate refractoriness (La-Sm and Tm) are uniformly enriched. This pattern cannot be formed by evaporation alone and has been taken as evidence that condensation processes occurred in the early solar system.

The chemical fractionation of REEs recorded by CAIs was pervasive in the early solar system and affected planetary bodies at all scales. For example, the Earth and many meteorite parent-bodies display a resolvable depletion (~−4.5%) in the abundance of Tm relative to CI chondrites, which is interpreted to reflect the heterogeneous distribution in the solar nebula of refractory dust carrying group II REE patterns marked by large Tm excesses (~+200 to +5400%) relative to neighboring REEs Er and Lu (*7*, *8*). After formation, CAIs experienced further processing, which is reflected in their textures and compositions. Some CAIs were reheated and experienced melting and partial vaporization, which obscured signatures arising from solar nebula condensation (*9*–*12*). Others, in particular, fine-grained CAIs, never experienced melting and provide a more faithful record of solar nebula condensation. Because of their porous nature, fine-grained CAIs experienced extensive alteration, which modified their composition and mineralogy (*13*). For elements that are fluid-immobile and refractory, this is, however, not a problem. Available Ti and Sr isotopic data of fine-grained inclusions indicate that kinetic processes were at play when fine-grained CAIs formed, but interpretation of these data in terms of evaporation/condensation processes is ambiguous (*14*–*16*).

REEs are ideally suited for testing the theory of equilibrium condensation of the solar nebula because they are relatively fluid immobile and display a range of 50% condensation temperatures that encompass the inferred formation temperature of CAIs (*17*), and their condensation behaviors are relatively well constrained. Although REE patterns can be explained by equilibrium condensation from gas of solar composition under a total H_2 pressure typical of the solar nebula of 10^{-5} to 10^{-3} bar (*15*, *18*–*20*), abundances alone cannot easily tell if kinetic processes were at play during either evaporation or condensation. The reason is that evaporation kinetics are also governed by thermodynamics and equilibrium vapor pressures through the Hertz-Knudsen equation (*21*). Isotopes are highly sensitive to disequilibrium during evaporation and condensation (*9*, *22*–*28*).

[1]Origins Laboratory, The University of Chicago, 5734 South Ellis Avenue, Chicago, IL 60637, USA. [2]Department of the Geophysical Sciences, Enrico Fermi Institute, Chicago Center for Cosmochemistry, The University of Chicago, 5734 South Ellis Avenue, Chicago, IL 60637, USA. [3]The Isotoparium, Division of Geological and Planetary Sciences, California Institute of Technology, 1200 E. California Blvd, Pasadena, CA 91125, USA. [4]Department of Earth and Environment, Boston University, 685 Commonwealth Avenue, Boston, MA 02215, USA. [5]School of Geography, Earth and Environmental Sciences, Victoria University of Wellington, Wellington 6140, New Zealand. [6]IMPMC, CNRS, UMR 7590, Sorbonne Universités, Université Pierre et Marie Curie, Muséum National d'Histoire Naturelle, CP 52, 57 rue Cuvier, Paris F-75231, France. [7]Advanced Photon Source, Argonne National Laboratory, 9700 South Cass Avenue, Argonne, IL 60439, USA.
*Corresponding author. Email: jingya@uchicago.edu

They can therefore be used to understand the physicochemical pathway of CAI formation.

During condensation from a supersaturated medium, the light isotopes will impinge on mineral surfaces more frequently than the heavy isotopes, resulting in a light isotope enrichment in the condensed phase relative to the vapor. Conversely, during evaporation in an undersaturated medium, the light isotopes will be more readily lost than the heavy ones, resulting in a heavy isotope enrichment of the condensed phase relative to the vapor. If either evaporation or condensation takes place in a vapor whose partial pressure is in close equilibrium with the condensed phase, the fluxes in and out of the condensed phase will be nearly balanced and the vapor and solid/liquid will be in isotopic equilibrium. Given the elevated temperature involved in CAI formation, the expectation is that equilibrium isotopic fractionation should be small. As such, measuring the isotopic composition of REEs in CAIs displaying group II REE patterns should theoretically (i) reveal if these CAIs formed under equilibrium conditions and if they did not (ii) allow the roles played by evaporation and condensation processes to be resolved, which can help tie CAI formation and chemical fractionation of refractory elements to phenomena happening around young stellar objects.

Here, we report the isotopic compositions of eight REEs in eight CAIs (including seven fine-grained ones with group II REE patterns) from the Allende CV chondrite (Table 1). These measurements were made possible using a fluoropolymer pneumatic liquid chromatography (FPLC) system [fig. S1; (*29*, *30*)] to separate the REEs from one another. The REEs analyzed are Ce, Nd, Sm, Eu, Gd, Dy, Er, and Yb. The other polyisotopic REEs La and Lu were not measured, as these have only two stable isotopes, one of which is extremely minor in abundance (0.09% for ^{138}La and 2.6% for ^{176}Lu). Furthermore, large ^{138}La anomalies of probably nucleosynthetic origin have been reported (*31*), which would hamper the detection of mass-dependent fractionation for La. In CAIs with group II REE patterns, we observe substantial stable isotopic fractionations of the REEs indicative of disequilibrium formation pathways.

RESULTS

The abundances of Ce, Nd, Sm, Eu, Gd, Dy, Er, and Yb in group II CAIs [table 2 in (*15*)] are normalized to Sm abundance and CI chondrites (*32*) and plotted in Fig. 1A in order of increasing refractoriness according to their condensation temperatures under solar nebula conditions in 10^{-4} bar H_2 (see fig. S2 for the REE abundance pattern plotted as a function of atomic mass) (*17*). Both the least refractory (Eu and Yb) and most refractory REEs (Gd, Dy, and Er) are depleted, while the moderately refractory REEs (Ce, Nd, and Sm) display uniform enrichment relative to CI chondrites, which are characteristics of group II patterns (*5*).

For a given REE, the isotopic fractionation is expressed as per mil per atomic mass unit (‰/amu) deviations relative to terrestrial standard solutions using the following notation (the φ superscript refers to the δ notation on a per atomic mass unit basis)

$$\delta^{\varphi}\mathrm{E}\ (‰/\mathrm{amu}) = \left[\frac{(^{i}\mathrm{E}/^{j}\mathrm{E})_{\mathrm{Sample}}}{(^{i}\mathrm{E}/^{j}\mathrm{E})_{\mathrm{Standard}}} - 1\right]\frac{1000}{m_i - m_j} \qquad (1)$$

where m_i and m_j are the atomic masses of isotopes ^{i}E and ^{j}E, respectively (e.g., Ce isotopic fractionation δ^{φ}Ce in ‰/amu is reported as $\delta^{142/140}$Ce divided by the atomic mass difference 142 − 140 = 2). The reason for expressing isotopic variations on a per mil per amu basis is that the magnitude of mass-dependent fractionation of an element scales to first order with the difference in mass of the isotopes involved, so this notation allows easier comparison of the isotopic variations of several REEs covering different mass ranges. The terrestrial standard solutions used for normalization in the δ^{φ}E notation have isotopic compositions that are close to those of terrestrial basalts, which are presumably close to the bulk Earth values [Table 1; (*33*)]. The REE isotopic compositions in group II CAIs (Table 1) are plotted in order of increasing refractoriness in Fig. 1B. The most refractory REEs (Gd, Dy, and Er) show substantial negative stable isotopic fractionations ranging from 0 to −3.6‰/amu with averages approximately at −1.5‰/amu. The least refractory Eu and Yb and moderately refractory REEs Ce, Nd, and Sm range from −1 to +1‰/amu and define averages near 0. A CAI with a flat REE abundance pattern was also measured and shows isotopic compositions within ±0.25‰/amu of 0 for all REEs.

Although Sr has a nominal 50% condensation temperature (1464 K) that is ~100 K higher than that of Eu (1356 K) (*17*), the elemental enrichment factors of Eu and Sr in CAIs normalized to CI chondrites are tightly correlated, meaning that, during evaporation and condensation, the two elements have very similar behaviors (*16*). Comparing our new Eu isotopic analyses with previous Sr stable isotopic fractionation data measured on the same sample digestion using a double-spike approach shows that δ^{φ}Eu and δ^{φ}Sr also correlate closely over a range of δ^{φ}Sr values from −1.8 to +0.8‰/amu with a slope of 0.67 (Fig. 2A). This is further evidence that Eu and Sr have very similar behaviors during condensation in the nebula. Linear correlations between isotopic compositions were also observed for Ce and Nd versus Sm (with slopes of 0.90 and 1.13, respectively; Fig. 2B) and Dy versus Gd (with a slope of 1.40; Fig. 2C). The Ti stable isotopic fractionation in this set of CAIs was reported in (*15*) using sample-standard bracketing (SSB) and was remeasured in this study using the double-spike approach to achieve higher precision (table S1). The 50% condensation temperature of Ti is 1582 K under solar nebula conditions (at 10^{-4} bar total pressure of H_2), which overlaps with that of light REEs (LREEs) (*17*). The isotopic fractionation of Ti ranges from −0.2 to +1.0‰/amu but shows no clear correlation with any of the REEs. Because Ti is a major element in CAIs, its behavior during evaporation and condensation is likely to be decoupled from the REEs, which usually substitute into host minerals as trace elements. Correlation matrices showing all possible bivariate correlations for abundances and isotopes of the elements investigated in this set of CAIs are shown in fig. S3. The correlations highlighted above (Eu-Sr, Ce-Nd-Sm, and Dy-Gd) are the only ones that are statistically significant. Yb and Eu, which are among the least refractory REEs, are not correlated isotopically (Fig. 2D). The stable isotopic composition of U also does not correlate with that of any REE including Yb, whose abundance correlates with that of U [fig. S4; (*34*)].

Few data are available in the literature to compare with our results (*33*, *35*). A previous study (*33*) reported measurements of the stable isotopic compositions of Er and Yb in a variety of terrestrial rocks and bulk meteorites. They found limited variations in meteorites, which span ~0.3‰/amu for δ^{φ}Yb and ~0.15‰/amu for δ^{φ}Er. The isotopic variations documented in CAIs are much larger, spanning ~0.7 and ~3.6‰/amu for Yb and Er, respectively. The largest isotopic variations are found in the least REE-enriched CAIs, which contribute the least to the bulk inventory of these elements in CAI-bearing

Table. 1. Stable isotopic fractionations of REEs in a geostandard and CAIs. The δ^{φ}E values are per mil/amu variations relative to terrestrial standards (OL-REEs) calculated using Eq. 1 applied to $^{142}Ce/^{140}Ce$, $^{146}Nd/^{144}Nd$, $^{152}Sm/^{148}Sm$, $^{153}Eu/^{151}Eu$, $^{158}Gd/^{156}Gd$, $^{164}Dy/^{162}Dy$, $^{168}Er/^{166}Er$, and $^{174}Yb/^{172}Yb$ ratios.

Isotopic fractionation (‰/amu)

Sample	CAI name	δ^{φ}Ce			#*	δ^{φ}Nd			#*	δ^{φ}Sm			#*	δ^{φ}Eu			#*	δ^{φ}Gd			#*	δ^{φ}Dy			#*	δ^{φ}Er			#*	δ^{φ}Yb		
BCR-2		0.02	±	0.01	10	−0.01	±	0.02	15	0.00	±	0.01	9	0.01	±	0.03	4	0.02	±	0.03	10	0.02	±	0.03	8	−0.05	±	0.02	8	0.02	±	0.05
TS32		0.24	±	0.06	1	−0.03	±	0.05	4	−0.01	±	0.06	2	−0.19	±	0.05	2	−0.02	±	0.03	2	−0.02	±	0.07	3	−0.02	±	0.13	2	0.04	±	0.07
ME-3364-25.2	FG-FT-3	0.01	±	0.04	9	−0.14	±	0.01	9	−0.09	±	0.06	5	−1.09	±	0.05	1	−0.89	±	0.03	1	−1.04	±	0.07	1	−1.00	±	0.02	1	−0.33	±	0.07
ME-2639-16.2	FG-FT-4	0.81	±	0.04	12	1.1	±	0.01	8	0.8	±	0.06	3	−0.01	±	0.05	2	−0.61	±	0.03	2	−0.58	±	0.06	2	−2.89	±	0.11	1	−0.12	±	0.07
ME-2639-49.7	FG-FT-6	−0.03	±	0.02	9	−0.57	±	0.08	5	−0.37	±	0.06	2	−0.42	±	0.02	1	−1.03	±	0.07	3	−1.67	±	0.04	3	−2.02	±	0.05	1		±	
ME-2639-51.1	FG-FT-7	0.42	±	0.03	9		±			0.07	±	0.06	5	−0.58	±	0.05	1	−1.28	±	0.03	3	−1.64	±	0.07	2	−2.24	±	0.02	1	−0.66	±	0.07
AL3S5	FG-FT-8	0.51	±	0.01	9	−0.02	±	0.03	8	0.07	±	0.01	9	0.04	±	0.11	2	−2.26	±	0.01	9	−3.07	±	0.01	9	−1.89	±	0.11	2	0.01	±	0.05
AL4S6	FG-FT-9	−0.82	±	0.01	9	−0.93	±	0.02	11	−0.97	±	0.02	9	0.73	±	0.04	6	−1.05	±	0.07	5	−1.10	±	0.02	7	0.08	±	0.04	6	−0.32	±	0.01
AL8S2	FG-FT-10	0.35	±	0.05	5	−0.16	±	0.08	3	−0.03	±	0.05	1	−1.03	±	0.11	1	−0.35	±	0.07	2	−0.53	±	0.04	1	−3.63	±	0.05	1		±	
ME-2639-16.2	FG-FT-4†	0.96	±	0.07	5	0.68	±	0.04	8	0.88	±	0.06	5	0.03	±	0.06	4	−0.57	±	0.03	6	−0.55	±	0.02	6	−2.90	±	0.11	2	−0.12	±	0.05
AL3S5	FG-FT-8†	0.70	±	0.01	8	−0.01	±	0.01	15	0.11	±	0.01	11	0.13	±	0.06	3	−2.28	±	0.02	10	−3.08	±	0.02	8	−1.88	±	0.11	2	−0.05	±	0.15
AL4S6	FG-FT-9†	−0.62	±	0.07	5	−0.87	±	0.01	13	−0.84	±	0.02	7	0.82	±	0.06	3	−1.05	±	0.19	4	−1.15	±	0.06	5	0.01	±	0.11	5	−0.32	±	0.02

*Number of measurements. †Replicates subjected to substantial loss of REEs during Mo chemistry and not used for data interpretation.

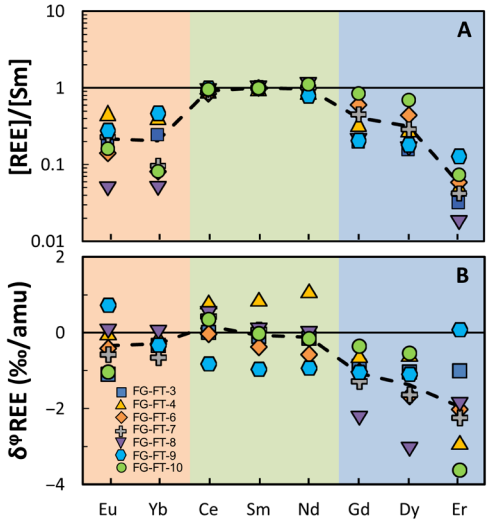

Fig. 1. Abundances and stable isotopic fractionations of REEs ordered by increasing refractoriness (from the least refractory on the left to the most refractory on the right). (**A**) Abundances of REEs in seven fine-grained CAIs with group II REE patterns [table 2 in (*15*)] normalized to Sm abundance and chondrites (*7*). Orange, green, and blue shades are least refractory, moderately refractory, and most refractory REEs, respectively. Each symbol corresponds to one CAI. The dashed line is the average abundance of seven CAIs for each REE. (**B**) Isotopic fractionations of REEs in the same seven CAIs (Table 1). The dashed line is the average isotopic fractionations of the seven CAIs analyzed. Note that one CAI with a flat REE abundance and isotopic pattern (TS32) is not plotted here (Table 1). See Table 1 caption and Eq. 1 for details on the δ^{φ} notation.

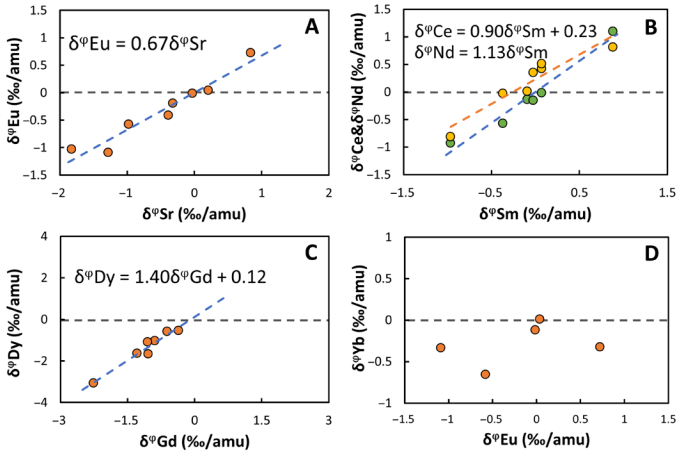

Fig. 2. Relationship of stable isotopic fractionations of REEs. (**A**) Correlation of isotopic fractionations Eu versus Sr in seven CAIs with group II pattern. (**B**) Ce and Sm versus Nd. (**C**) Dy versus Gd. (**D**) Yb versus Eu. See Table 1 caption and Eq. 1 for details on the δ^{φ} notation. The REE data are from Table 1, while the Sr data are from (*16*).

meteorites. This could explain the limited isotopic variations documented by (*33*) in bulk meteorites. Another study (*35*) reported measurements of the Sm and Eu isotopic compositions of several chondrites and CAIs. They found limited variations, with δ^{φ}Sm and δ^{φ}Eu values in CAIs reaching ~+0.34 and −0.34‰/amu, respectively. The δ^{φ}Sm and δ^{φ}Eu values measured here span ranges of ~1.9 and 1.8‰/amu, respectively. The difference could be due to the fact that we focused on CAIs with highly fractionated REE patterns, while (*35*) may have measured samples with mostly flat (unfractionated) REE abundance patterns [the REE pattern is known for only one of the four CAIs that they measured and it is a flat group I (*5*)]. Highly fractionated group II REE patterns are most commonly found in fine-grained CAIs that are difficult to extract from meteorites, and it is conceivable that the CAIs studied by (*35*) were of the more readily extractable coarse-grained kind. We measured negligible isotopic fractionation in one CAI with a flat REE abundance pattern (TS32; Table 1).

DISCUSSION

A kinetic origin for the isotopic fractionation of the REEs

Although the various isotopic patterns for each group II CAI reflect their unique formation histories, they still share similarities, among which the most distinctive feature is that the most refractory REEs (Gd, Dy, and Er) are all enriched in the light isotopes with average isotopic compositions of approximately −1.5‰/amu. In contrast, the less refractory REEs show smaller isotopic variations, centered around 0 (Fig. 1B).

The isotopic fractionations of the REEs could be due to equilibrium or kinetic processes, or a combination of both during evaporation and condensation. The extent of equilibrium isotopic fractionation can be estimated based on thermodynamic considerations. During evaporation or condensation of CAIs under solar nebula conditions, REEs in minerals (presumably hibonite or perovskite) exist as 3+, except for Eu, for which a substantial fraction may exist as 2+ (*36*). In the vapor, La, Pr, Nd, Gd-Er, and Lu are predominantly composed of monoxides (2+), with less than 15% present as monatomic gas (0 oxidation state). Gaseous Eu and Yb are nearly all monatomic, while Sm and Tm are predominantly monatomic species with only moderate fractions (~30 and 5%, respectively) of monoxides. The majority (i.e., ~90%) of Ce exists in the vapor as CeO_2 (4+) and the rest as CeO (2+). There are no data or calculations that we are aware of to estimate equilibrium isotopic fractionation between Ce^{4+} in the vapor and Ce^{3+} in minerals, but we can estimate the other fractionation factors. All trivalent REEs have similar geochemical behavior, and it is likely that they form chemical bonds of similar strengths. The technique of nuclear resonant inelastic x-ray scattering (NRIXS) applied to the Mössbauer isotope ^{151}Eu in solid EuO and Eu_2O_3 gives force constants of Eu^{2+} and Eu^{3+} of 114 and 196 N/m, respectively (*37*). The formula that relates reduced partition function ratio to force constant for Eu is [(*37*) and references therein]

$$1000\ln\beta_{\mathrm{Eu}}^{\varphi} = 193\frac{\langle F_{\mathrm{Eu}}\rangle}{T^2} \quad (2)$$

where $1000\ln\beta_{\mathrm{Eu}}^{\varphi} = 1000\ln\beta_{\mathrm{Eu}}^{1/(m_i-m_j)}$ is the equilibrium fractionation factor in ‰/amu in the compound of interest relative to monoatomic gas, $\langle F_{\mathrm{Eu}}\rangle$ is the force constant in N/m, and T is the temperature in K. Using this formula, we estimate that at 1750 K, relevant to CAI formation, the equilibrium isotopic fractionation between Eu^{2+} and Eu^{3+} in solid and monatomic Eu in gas will be +0.007 and +0.012‰/amu, respectively. The force constant of gaseous EuO is not known but it can be calculated using the formula relating vibration wave number to bond force constant for diatomic molecules

$$\langle F_{\mathrm{Eu}}\rangle = 4\pi^2 m^* c^2 \nu^2 \quad (3)$$

where $\nu = 668\ cm^{-1}$ is the vibration wave number of EuO in an argon matrix (*38*), $c = 299792458$ m/s is the speed of light, and $m^* = 2.404 \times 10^{-26}$kg/amu is the reduced mass of EuO. This gives a directionally averaged force constant of 127 N/m, corresponding to $1000\ln\beta^{\varphi}_{Eu} = +0.008$‰/amu for gaseous EuO. The equilibrium isotopic fractionations between Eu^{2+} and Eu^{3+} in solid and EuO in gas at 1750 K are therefore −0.001 and − 0.004‰/amu, respectively. Regardless of the speciation of the REEs in the vapor or minerals, the expected equilibrium isotopic fractionation is always smaller than ~0.02‰/amu (Fig. 3). Even if a Rayleigh distillation was involved in the depletion of some REEs relative to others, the resulting isotopic fractionation would be 0.1‰/amu at most, assuming a depletion factor of 100. This calculation shows that equilibrium isotopic fractionation cannot explain the REE isotopic fractionation observed in group II CAIs, thus demonstrating that these CAIs are not simple solar nebula equilibrium condensates but that kinetic processes associated with evaporation and/or condensation played some role.

Isotopic fractionation of the most refractory REEs

As discussed in the Introduction, the isotopic fractionation experienced by solids or liquids during evaporation and condensation is characteristic of the process involved and the saturation conditions. In the canonical view of the origin of the group II pattern, the most refractory REEs are sequestered in ultrarefractory grains that are removed from the system. Below, we discuss several scenarios for the removal of this ultrarefractory component and show how only the partial evaporation scenario (iii) is viable.

(i) If these ultrarefractory grains (distinct from the refractory CAIs investigated here) condensed under supersaturated conditions, the vapor left behind would have been isotopically heavy. This signature would have been imparted to the highly refractory REEs in CAIs condensed from this vapor, which is the opposite to what is observed (Fig. 1B).

(ii) An alternative scenario is that ultrarefractory grains formed in near-equilibrium conditions, leaving behind vapor depleted in the most refractory REEs but with near-normal isotopic composition. If group II CAIs condensed under supersaturated conditions from such unfractionated gas, the most refractory REEs could have acquired a light isotopic composition, consistent with observations. However, for isotopic fractionation to be expressed during condensation, mass balance requires that only a fraction of the refractory REEs should be condensed. In that case, we would expect a substantial fraction of the more volatile moderately refractory REEs (Ce, Nd, and Sm) to remain in the gas residue, leading to elemental depletion and isotopic fractionations of moderately refractory REEs in group II CAIs, which is not observed.

(iii) The most plausible scenario is therefore that the refractory heavy REE acquired their light isotope enrichments by near-complete condensation of vapor produced by a previous stage of nonequilibrium evaporation that left behind material akin to ultrarefractory grains.

The magnitude of stable isotopic fractionation during partial evaporation depends on the fraction of the target element left in the residue, the kinetic fractionation factor that describes the difference in evaporation rates for two isotopes, and the degree of undersaturation of the vapor (*9*, *22*, *25*). The finding of large kinetic isotopic fractionation for refractory REEs Gd and Dy means that evaporation took place in a medium that was undersaturated, which provides constraints on the time scale of this evaporation episode. If the surrounding vapor is highly undersaturated, evaporation is faster and isotopic fractionation is larger than when vapor is near equilibrium and the fluxes in and out the residue are nearly balanced.

To quantify the evaporation time scale, we have built a simple scenario (Fig. 4A; see the Supplementary Materials for details) whereby ultrarefractory grains of equal sizes are evenly distributed in space, and evaporation is driven by a temperature increase $T(t) = T_{h,0} + \Phi_h t$, where $T_{h,0}$ is the initial temperature and Φ_h is the heating rate (a positive number). The value of $T_{h,0}$ has little influence on the model result provided that it is low enough that all REEs are fully condensed at the beginning of the calculation. In our simulations, we adopt a value of 1350 K. Evaporation happens in a closed system until a time (temperature) when ultrarefractory grains are physically separated from the vapor. Some meteorites like Allende display a group II REE pattern at a bulk scale (*7*, *8*, *39*), supporting the view that ultrarefractory inclusions with REE patterns complementary to group II were physically separated at large scales from lower temperature refractory materials. We define the time scale of the evaporation event as the time span between 5% evaporation of the least refractory REE (Eu) and the time of ultrarefractory solid removal.

This model shares similarities with those applied to closed-system condensation/evaporation and chondrule formation (*22*–*24*, *26*, *27*). The chemical depletions and isotopic fractionations of the REEs evaporated depend on the heating rate and duration of the evaporation episode. If temperature increases slowly, the vapor pressure is always close to equilibrium, evaporation is slow, and isotopic fractionation approaches equilibrium, which is small at the temperatures considered. Conversely, if temperature increases rapidly, evaporation

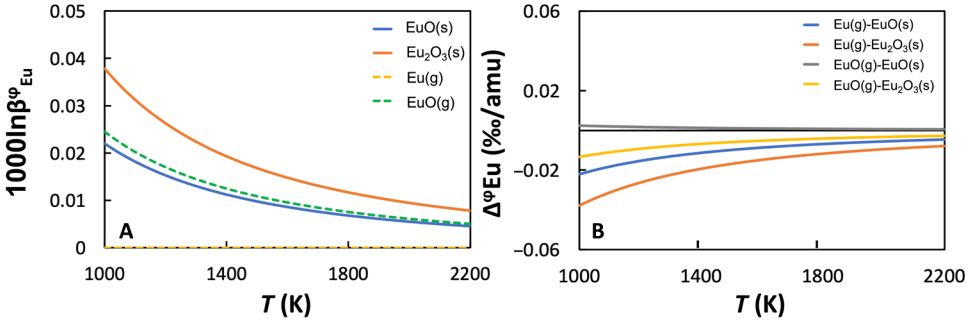

Fig. 3. Equilibrium isotopic fractionations of Eu. (**A**) Calculated reduced partition function ratios (in ‰/amu) of Eu compounds as a function of temperature. (**B**) Equilibrium isotopic fractionation between gas and solid phases of Eu as a function of temperature. See text for details.

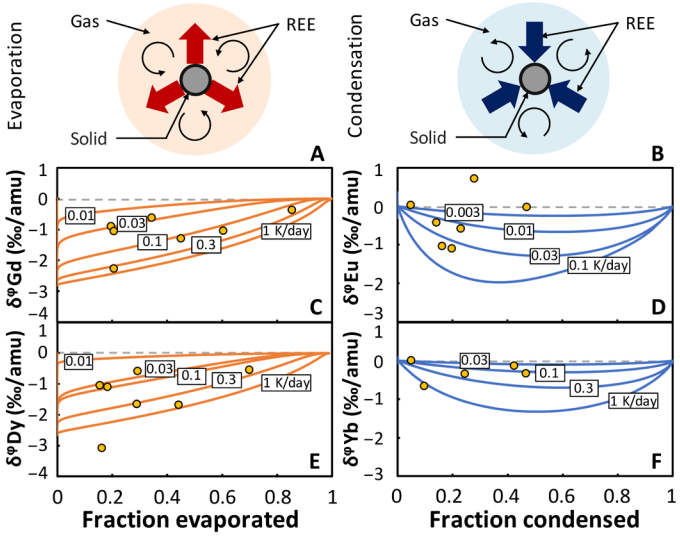

Fig. 4. Trajectories of chemical depletion and isotopic fractionation in the evaporation (left) and condensation (right) stages considered to explain the composition of group II CAIs (see text and the Supplementary Materials for details). Schematics of the models envisioned for evaporation (**A**) and condensation (**B**). (**C**) Gd and (**E**) Dy isotopic fractionations and depletions during closed-system evaporation for different heating rates. (**D**) Eu and (**F**) Yb isotopic fractionations and depletions during closed-system condensation for different cooling rates. The labels on the curves are the heating rates (evaporation) and cooling rates (condensation) used in the calculations.

is fast but insufficient to keep up with the increasing equilibrium vapor pressure, leading to undersaturation and light isotope enrichment in the vapor (*22*). The two unknowns of the model are the heating rate and duration, which can be solved for using the two observables chemical depletion and isotopic fractionation of Gd and Dy—the two highly refractory REEs most affected by this evaporation episode.

The fractions of Gd and Dy evaporated from the ultrarefractory residue can be estimated for each CAI using their abundances normalized to chondrites over that of the moderately refractory REE Sm, which, like other moderately refractory REEs, would have been lost quantitatively from the precursors of ultrarefractory inclusions and fully condensed in the CAI. We have used thermodynamic modeling to calculate the isotopic fractionations and depletions of Gd and Dy for different heating rates and compare model predictions with our measurements (details of the modeling are provided in the Supplementary Materials). The thermodynamic data, oxygen fugacity, and number of moles of Ca condensed per unit volume of the system used for modeling evaporation are from (*15*) assuming that the mineral host of REEs during evaporation is hibonite. Although hibonite is rare in the fine-grained CAIs that we studied, we have adopted it as the REE solid carrier because (i) hibonite is the highest temperature mineral that incorporates substantial REEs, (ii) it is the only likely REE host phase over a 55-K range (*40*), (iii) it could have been present as a precursor mineral before disappearing by reaction with the vapor during cooling and is found in some ultrarefractory inclusions in CM chondrites (*6*), and (iv) perovskite is another option but it cannot explain Tm anomalies (*19*). We find that the heating rates of Gd (Fig. 4C) and Dy (Fig. 4E) in most CAIs fall in the range of ~0.03 to 0.3 K/day for a duration of the evaporation episode of hundreds to thousands of days.

Stable isotopic fractionation of the least refractory REEs (Eu and Yb)

The uniform enrichment of the moderately refractory REEs and the relative depletion of the least refractory REEs can potentially be explained by either evaporation or condensation. In the evaporation scenario, the vapor produced by evaporation of an ultrarefractory component as described above was quantitatively condensed in a second generation of refractory inclusions that were subsequently reheated and lost the least refractory REEs (Eu and Yb) to the vapor. In the condensation scenario, during cooling of the parcel of vapor produced by evaporation of an ultrarefractory component, the moderately refractory LREEs were quantitatively condensed but vapor was separated from the solid before the least refractory REEs condensed.

Overall, Eu and Yb show limited stable isotopic fractionations, with most Yb data displaying negative δ^{φ}Yb values consistent with partial condensation being the dominant process. A likely explanation for the limited isotopic variations but large elemental depletions of Eu and Yb is that their condensation took place under near-equilibrium conditions. The degree of isotopic fractionation during condensation (*14*, *22*, *25*, *28*) is related to the degree of chemical depletion, the kinetic isotopic fractionation factor associated with condensation, and the degree of supersaturation. As with evaporation, isotopic fractionation during condensation can provide constraints on the time scale of this condensation episode. If the surrounding vapor is highly supersaturated, condensation is faster and isotopic fractionation is larger than when vapor is near equilibrium and the fluxes in and out the condensate are nearly balanced.

To quantify the condensation time scale, we have built a simple scenario (Fig. 4B; see the Supplementary Materials for details) whereby vapor produced during the first evaporation episode condenses in a second generation of refractory inclusions, and condensation is driven by a temperature decrease $T(t) = T_{c,0} + \Phi_c t$, where $T_{c,0}$ is the initial temperature and Φ_c is the cooling rate (a negative number). The value of $T_{c,0}$ has little influence on the model result provided that it is high enough that all REEs are fully evaporated at the beginning of the calculation. In our simulations, we adopt a value of 1700 K. Condensation happens in a closed system [also see (*22*, *26*)] until a time or temperature at which the vapor is dissipated and the remaining least refractory REEs are lost. We define the time scale of the condensation event as the time span between 5% condensation of highly refractory REE (Dy) and the time of gas dissipation. The chemical depletions and isotopic fractionations of the condensed REEs depend on the cooling rate and duration of the condensation episode. If temperature decreases slowly, the vapor pressure is always close to equilibrium, condensation is slow, and isotopic fractionation approaches equilibrium, which is small at the temperatures considered. Conversely, if temperature decreases rapidly, condensation is fast but insufficient to keep up with the decreasing equilibrium vapor pressure, leading to oversaturation and light isotope enrichment in the condensate (*22*). Moderately refractory REEs are present in near-chondritic proportions and show little isotopic fractionations (Fig. 1A and fig. S1), so they were most likely quantitatively condensed during this stage. Highly refractory REEs were also quantitatively condensed. The only REEs affected by this stage are the least refractory Eu and Yb. Despite their large elemental depletions (Fig. 1A), these REEs show little isotopic fractionations (Fig. 1B), meaning that cooling must have been protracted and condensation occurred under near-equilibrium conditions. We calculated the cooling rate (Φ_c) and overall duration t (time of vapor dissipation after the onset of condensation) needed

to explain the large depletions and small isotopic fractionations of Eu and Gd depletions (Fig. 4D). We find that the cooling rates relevant to most CAIs are lower than 0.1 K/day for Eu and 1 K/day for Yb (Fig. 4F). The duration of this condensation episode must have been at least a few hundreds of days.

Evaporation-condensation scenario inferred from REE isotope systematics

The isotopic compositions and depletions of the most refractory and least refractory REEs are most readily explained in the context of a two-stage evaporation-condensation scenario (Fig. 5).

In the first stage, nebular dust with chondritic REE abundances was subjected to closed-system evaporation. The least refractory and moderately refractory REEs were quantitatively vaporized, and the vapor inherited the isotopic composition of the solid precursor for these elements. The most refractory REEs were only partially vaporized. The partial evaporation of the most refractory REEs induced substantial negative isotopic fractionations in the vapor because the lighter isotopes evaporated more readily than heavy ones during kinetically controlled evaporation.

In the second stage, vapor was physically isolated from the solid residue and subsequently condensed to form CAIs with group II REE pattern under near-equilibrium conditions. The most refractory REEs and the moderately refractory REEs were completely condensed at this stage and inherited the abundance and isotopic compositions from the gas phase. The least refractory REEs were only partially condensed, which resulted in their depletion in CAIs. The limited isotopic fractionations observed in the least refractory REEs required that the cooling that induced condensation must have been slow enough to maintain near-equilibrium conditions.

We have modeled the REE abundance and isotopic pattern predicted by this two-stage scenario and it can quantitatively reproduce the composition of group II CAIs. In this two-stage scenario, the elemental abundances of the most refractory REEs were fractionated due to previous isolation of an ultrarefractory component, which had an REE pattern complementary to group II pattern except for Eu and Yb. Such ultrarefractory REE patterns are rare but are found in a few refractory inclusions from carbonaceous chondrites such as Murchison and Ornans [e.g., (*41*, *42*)]. A prediction of our model is that ultrarefractory inclusions should be evaporation residues, and as such, they should be enriched in the heavy isotopes of the REEs, especially for the least refractory and moderately refractory (Ce, Nd, Sm, Eu, and Yb). The view that ultrarefractory inclusions are evaporation residues agrees with the W depletion measured in an ultrarefractory inclusion from Ornans, as this feature requires relatively oxidizing condition, which is more easily achieved through evaporation than condensation of solar nebula gas (*41*). Analyzing the stable isotopic fractionation of REEs in these refractory inclusions will shed light on their genetic relationship with group II CAIs.

Early solar system events responsible for the formation of CAIs

According to the two-stage scenario outlined above, CAIs characterized by group II patterns were formed by heating above 1600 K for hundreds to thousands of days of dust with initially chondritic REE composition, followed by cooling of the vapor formed by the first evaporation stage for at least a few hundreds of days. It is difficult to tie this thermal history to specific early solar system events, but we speculate that such a heating history could have taken place during rapid solar outbursts when the young Sun went through EXor or FUor events akin to those documented in remote stars. EXors are a group of pre–main-sequence stars characterized by intense, episodic increases in brightness separated by quiescent periods (*43*). They are named after the prototype EX Lupi, which is a low-mass, Sun-like young star located at Lupus cloud (*44*). FUors are eruptions in FU Orionis objects, another group of pre–main-sequence stars that see episodes of brightening of higher intensity and longer duration than EX Lupi (*43*, *45*). Observations of accretion tracers such as spectral lines and veiling indicate that these large, repetitive outbursts are caused by episodic increase of mass accretion from the protoplanetary disk onto the star. Taking EX Lupi as an example, the typical time scale of the outburst ranges from several months to a few years, during which the brightness of the star can increase by two to five magnitudes (*44*). The brightness during the outburst can fluctuate substantially, possibly leading to rapid temperature swings in the inner region of the protoplanetary disk.

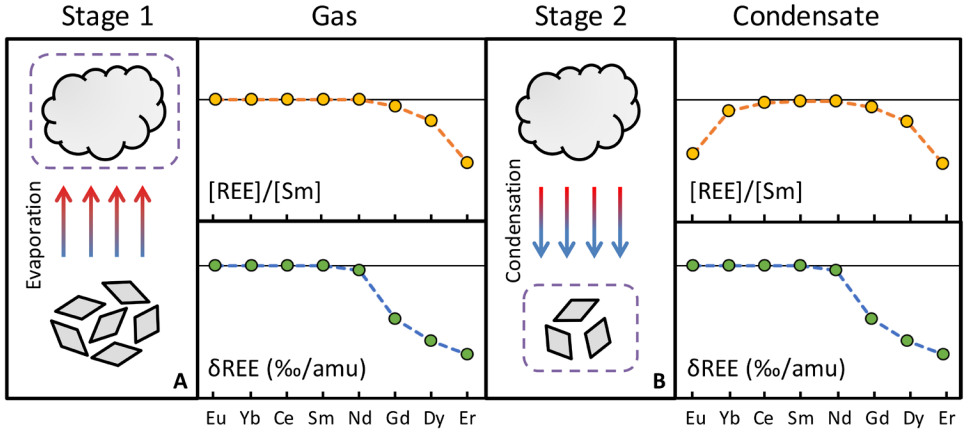

Fig. 5. Schematics of group II REE fractionation in CAIs. (**A**) Stage 1: Nebular dust with chondritic proportions of the REEs evaporates in an undersaturated medium, which leaves behind an ultrarefractory residue and produces vapor depleted in the heavy most refractory REEs that are also characterized by light isotope enrichments. (**B**) Stage 2: The vapor from stage 1 partially condenses. The highly refractory (HREEs except Tm and Yb) and moderately refractory (LREEs and Tm) are completely condensed. The least refractory REEs Eu and Yb remain in the gas and are not completely condensed. The condensation during that stage occurs in near-equilibrium conditions, resulting in minimal isotopic fractionation for Eu and Yb.

The increase in brightness during FUors and EXor outbursts could be associated with large scale transport and intense thermal processing of preexisting dust in the central region of the protoplanetary disk (*46*, *47*). This is supported by the discovery in 2008 of in situ formation of crystalline silicates in one of the largest outbursts that happened in the circumstellar disk of EX Lupi (*48*). Objects like CAIs might have been subjected to similar thermal processing near the protostar during FUors or EXor outbursts. The increased luminosity of the Sun and internal dissipation associated with higher mass flux through the disk would both lead to higher temperatures in the solar nebula. We propose that FUors and EXor outbursts or similar events happened in the early solar system and are responsible for the formation of group II CAIs and refractory dust of similar composition.

The periods of the optical light luminosity of FUors and EXor outbursts range from hundreds of days to 100 years (*43*, *45*). The timescale for dust transport between cooler and hotter parts of the disk during FU Orionis events could be as low as tens of years (*46*, *47*). These timescales are consistent with the time required for evaporation of the most refractory REEs and the condensation of the least refractory REEs. During the outburst or passage through the hot inner part of the disk, only part of the most refractory REEs (and all the least refractory and moderately refractory REEs) was vaporized at the peak luminosity, leading to substantial light isotope enrichments of the most refractory REEs in the vapor. When the outburst subsided or when CAIs moved outwards, most REE condensed except the least refractory REEs, prohibited by the relatively high ambient temperature. The chemical and isotopic compositions of CAIs with group II patterns might reflect the influence of several cycles of evaporation and condensation before final condensation in refractory inclusions. During or after the FUors or EXor outburst, newly formed CAIs would have been distributed to the outer regions of the solar system through extensive radial transport, where they were incorporated in comets and other low-temperature outer solar system objects (*49*–*52*).

MATERIALS AND METHODS

Sample selection and digestion

The samples used in this study were selected from a group of CAIs that were previously studied by (*34*). The sampling and digestion procedures are described in detail in the supplementary section of (*34*) and only briefly summarized here.

The CAIs studied by (*34*) were mostly fine-grained CAIs extracted from a few Allende slabs using a stainless steel dental tool. The mass of the CAIs ranged from 15 to 440 mg [table S2 in (*34*)]. A small chip of each CAI was taken and mounted in epoxy for chemical and petrographic characterization. Most minerals have a grain size on the order of about 10 μm and are mostly composed of spinel, pyroxene, sodalite, and nepheline, with minor and variable amounts of grossular, melilite, and olivine. One coarse-grained CAI (TS32) was characterized in a separate study and provided in powder form. It is primarily composed of melilite, pyroxene, anorthite, and spinel, with a small amount of grossular and perovskite (*53*). The main mineral carriers of REEs in TS32 are pyroxene, perovskite, and melilite (*53*). Fine-grained CAIs in Allende have been extensively altered, and to our knowledge, the distribution of REEs in these objects has not been studied.

Powdered samples were digested in a mixture of HF/HNO_3 in 3:1 proportion with a few drops of $HClO_4$ added. The samples in acid were placed on a hot plate at 160°C for 2 weeks, after which each sample was evaporated to dryness and redissolved in a 2:1 mixture of $HCl:HNO_3$ for 1 week on a hot plate. These steps were performed twice to ensure complete digestion. The samples were dried down and dissolved in concentrated HNO_3. All samples were then diluted in 3 M HNO_3 and centrifuged. No residue was visible. After dissolution, 80% of the sample was taken and processed through two U/TEVA columns for U extraction. The matrix cuts that contained all REEs were recovered after the U/TEVA chemistry.

REE extraction and FPLC elution

Approximately 30% of the matrix cut from the U/TEVA chemistry of (*34*) (equivalent to 24% fraction of the whole CAI) was passed through a prepacked TODGA column for extraction of the bulk REEs (*32*). The yields of this REE TODGA extraction step were near 100%. The bulk of the REE cut was then subjected to a two-step FPLC (*29*, *30*) elution to separate REEs from each other.

Another 40% from the same matrix cut of the U/TEVA chemistry was passed through a separate Mo chemistry, during which 40 to 90% of LREEs and 20 to 40% of heavy REEs (HREEs) were lost on columns. We analyzed the matrix cuts after Mo chemistry of three group II CAIs (FG-FT-4, 8, and 9) as replicates and compare their results with the same CAIs using the 30% matrix cut so as to assess the reproducibility of the isotopic analyses (see the "Assessment of data accuracy" section). The results from these replicates agree with those from the 30% matrix cut. They are not used, however, for data interpretation to avoid unnecessary influence of stable isotopic fractionation potentially induced by Mo chemistry.

As REEs behave very similarly during chromatography, difficulties in separating individual REEs from one another have hampered their isotopic analyses, especially for mass-dependent fractionation. Previous stable isotopic fractionation measurement of REEs has therefore focused on either Sm + Eu (*35*) or Er + Yb (*33*). To separate all target REEs, we developed an FPLC system at the University of Chicago [fig. S1; (*29*, *30*)]. The FPLC system was modified after publication of (*29*) to pneumatic actuation (*30*). Its most distinctive features are the following.

(i) The elution scheme is controlled by a computer via a LabView software interface, which allows one to run a fine-step gradient elution and mix as many as six reagents. Achieving a fine gradient elution like the one performed for the present study using traditional gravity-driven chromatography would be prohibitively labor intensive.

(ii) The liquid flow path is made of solid fluoropolymer. All parts related to elution are activated pneumatically using pressurized N_2 gas. Electronics are housed in a box that is positively pressurized and spatially isolated from the reagent reservoirs and the liquid flow path. This design reduces chances of contamination and ensures that the FPLC electronics are immune to acid fumes in the clean laboratory environment. A commercial high-performance liquid chromatography (HPLC) instrument would not survive under the harsh conditions needed to perform the elution.

(iii) The elution temperature can be adjusted from room temperature to 80°C through a water circulation system to achieve optimal and reproducible separation. The mixed reagents are forced through the column via pressurized high-purity N_2 gas (adjustable from 0 to 4 bar), making it possible to run elutions on extremely long columns (~70 cm for REE separation).

The sample solution is introduced into the FPLC system via a sample introduction loop composed of two fluoropolymer three-way valves. By changing the flow paths of the two valves, samples can be injected

and stored in a tube between the two valves, to be later connected to the major flow path of elution. The column used for FPLC elution of the REEs is 70 cm in length and 1.6 mm in internal diameter, filled with 1.4 ml of 25- to 50-μm Ln-Spec resin (Eichrom). The overall affinity of REEs for Ln resin decreases exponentially with increasing acid molarity (*29*). The REEs are eluted sequentially from low (La) to high (Lu) atomic number by ramping up the HCl molarity (see fig. S5A for the gradient elution used). The REE elution is performed at 70°C and consists of 94 steps of 2 ml each of increasing molarity from 0.1 to 6 M HCl. The flow rate of the elution is 0.17 ml/min. The total elution volume is 188 ml, and an elution lasts 16 hours. The eluting acid is automatically made by mixing Milli-Q (MQ) water with any of three HCl reservoirs (0.5, 2, and 6 M, respectively). The volumes of acid and water needed are automatically calculated in the LabView software and transferred into a mixing chamber using pneumatic positive displacement diaphragm metering pumps made of fluoropolymer. The elution curve was calibrated, and the elution cuts were defined using 10-ppm (parts per million) SPEX CertiPrep Multi-Element standard solution (fig. S5B). The eluted fractions were collected in fluoropolymer beakers mounted on a 16-position plastic-made, pneumatically actuated, and computer-controlled stage. The whole elution is automated and does not require operator attention after the sample is introduced.

All samples were subjected to a two-step FPLC elution at 70°C. In the first step, the bulk of the REEs was dried in a 6-ml PTFE beaker on a hot plate to a tiny drop (<5 μl) and then dissolved in 350 μl of MQ water. The dissolved sample was then loaded onto the FPLC system and subjected to a complete elution. The eluted reagents were collected in 32 cuts ranging from 2 to 20 ml each defined by knowledge gained on a previous calibration. Approximately 5% of each cut was taken and diluted for concentration measurement by multi-collector inductively coupled plasma mass spectrometry (MC-ICPMS). Elution cuts that contained a given REE were then combined based on the concentration measurements. The first elution was sufficient to separate most REEs with only minor overlap of Eu/Dy and Pr/Nd (<20% Dy in the Eu cut and 25% Pr in the Nd cut) and major overlap of Y/Er (fig. S5B), none of which showed clear isobaric and matrix effects according to our doping tests. To achieve a better separation, a second more specific elution step was performed. In this step, REEs that are not neighbor to each other were recombined and loaded onto the FPLC system. This involves four FPLC elutions (Ce, Nd, Sm/Gd/Er, and Eu/Dy/Yb) ranging from 92 to 188 ml (fig. S6). The overall yields of the two-step FPLC elution were higher than 95%. At the end of each elution, the column was cleaned by elution of 10 ml of 6 M HCl followed by 10 ml of MQ water at 70°C to eliminate cross contamination. The same resin batch was used for all the purifications with no adverse effect on the elution curves.

MC-ICPMS analysis and data reduction

The concentrations of all REEs and the isotopic compositions of Ce, Nd, Sm, Eu, Gd, Dy, Er, and Yb were analyzed at the University of Chicago on a Thermo Fisher Scientific MC-ICPMS upgraded to Neptune Plus specifications with the addition of an OnTool booster pump. The method for analyzing REE concentrations using an MC-ICPMS was discussed in detail in (*32*).

Isotopic analyses were done using the Neptune MC-ICPMS connected to an Apex Omega desolating nebulizer. A typical measurement consisted of 60-s take-up time, 60-s baseline, and 40 cycles with an integration time of 8.184 s per cycle. The cup configurations used for isotopic analyses of the REEs are provided in table S2. Most REEs were measured in static mode with the exception of Dy and Yb, for which a subconfiguration was used to monitor isobaric interferences. The subconfiguration was only measured twice at the beginning with integration times of 4.142 s each, and the average intensities were used to correct for isobaric interferences of the following 40 cycles in the main cup configuration after appropriate scaling. For example, correction of ^{162}Er and ^{164}Er on ^{162}Dy and ^{164}Dy, respectively, proceeds as follows: ^{166}Er is only measured in the subconfiguration, and ^{163}Dy is measured in both the main and subconfigurations. The ratio of intensities ^{166}Er/^{163}Dy in the two subconfigurations is calculated. This ratio is then multiplied by the ^{163}Dy intensity in the main configuration. The resulting main-configuration calculated ^{166}Er is then multiplied by the ratios ^{162}Er/^{166}Er and ^{164}Er/^{166}Er to subtract ^{162}Er and ^{164}Er from ion intensities at masses 162 and 164, which yields corrected ^{162}Dy and ^{164}Dy intensities.

To save sample solution, the idle time between cycles with the same configurations was set to zero, while the cycle after a configuration change was preceded by 10-s idle time. Isobaric effects from isotopes of neighboring elements were corrected by monitoring other isotopes of the same element, calculating intensities assuming natural abundance distribution, and subtracting the intensities from those of interfered isotopes.

As isotopic compositions of REEs in CAIs can be affected by nucleosynthetic anomalies and cosmogenic effects, we measured the isotopic composition of each REE through SSB. SSB is advantageous over the double-spike approach because one can distinguish mass-dependent fractionation from isotopic anomalies, which were observed in some REEs with more than two isotopes but are much smaller (and for the present purpose negligible) compared to mass fractionation. The overall yields on the columns were over 95%. Processing of a geostandard showed that no significant isotopic fractionation was introduced by column chemistry, at least compared to the large natural variations measured in the samples. As isotopic standards of REEs are not well established, especially for HREEs, we prepared isotopic standards (referred to as OL-REE series) using high-purity oxide in powder form from ESPI, which are available upon request from J.Y.H. or N.D. On average, LREEs were measured nine times bracketed by OL-REE isotope standard spaced apart by 300-s rinsing time. The concentration of the sample solution was usually 15 to 25 parts per billion (ppb), corresponding to a 3.5- to 10-V signal for the most abundant isotope (10 V for ^{140}Ce, 4 V for ^{142}Nd, and 3.5 V for ^{152}Sm). Eu and HREEs are depleted in CAIs with group II REE pattern and were usually measured one to six times at concentrations ranging between 1.5 and 10 ppb corresponding to 1.5 to 3 V for the most abundant isotope (2 V for ^{151}Er and ^{158}Gd, 3 V for ^{164}Dy, and 1.5 V for ^{166}Er and ^{174}Yb). Exceptions are Er measurement in FG-FT-3, 6, 7, and 10, which, due to the extreme Er depletion, were analyzed at 1.5 ppb with a signal of 0.25 V for ^{166}Er. Despite the low abundance for some REEs in CAIs, the total procedure blanks were more than two orders of magnitude lower than the sample amount. The substantial isotopic fractionation of highly depleted Er in some CAIs is also evidence that the sample measurements were not plagued by contamination from matrix surrounding the CAIs, as this would have shifted these Er isotopic compositions toward that of bulk Allende (~0‰/amu).

Isotope data reduction was done by copying the raw data into a spreadsheet and correcting for background and isobaric interferences. As documented in previous studies (*54*), isotopic anomalies and

cosmogenic effects are present for some REEs in CAIs but the variations are on the order of 0.1‰, which is negligible compared to the stable isotopic variations reported here. Therefore, the choice of ratio for reporting mass-dependent fractionation is not critical. For that purpose, we use in Eq. 1 the two most abundant isotopes for each REE.

The measurements were performed by SSB, whereby sample measurements (SMP) were interspersed with measurements of standards (STD) diluted to the same concentration as the sample, in the same acid as that used for diluting the sample. The reported $\delta^{\varphi}E$ values were calculated based on 1 to 12 (typically 5) STD-SMP-STD bracketings, using each time the average isotopic ratio of the two STD measurements to normalize the isotopic ratio of SMP. The confidence intervals for the isotopic fractionations are reported as 95% confidence intervals using the Student's *t* value and either the variability of sample $\delta^{\varphi}E$ values (i.e., all the sequences STD-SMP-STD) for those with six or more values or the variability of the $\delta^{\varphi}E$ values of standards bracketed by standards (i.e., all the sequences STD-SMP-STD-SMP-STD) for sample measurements with less than six values. The threshold of six repeat brackets is a trade-off between the following considerations: (i) It is difficult to robustly assess the SD based on a small number of bracketed sample measurements, and this can be estimated more robustly by using the isotopic dispersion of the numerous standard analyses performed during a session. (ii) The time between standard measurements is longer than that of samples bracketed by standards, which can detrimentally affect the SD, meaning that using the isotopic dispersion of the samples can be preferable.

Other than stable isotopic fractionation, REE isotopes in group II CAIs can be affected by isotopic anomalies induced by nucleosynthesis and, for isotopes with large neutron capture cross sections such as ^{149}Sm, ^{155}Gd, and ^{157}Gd, cosmogenic effects [see (*54*) for examples of cosmogenic effects in CAIs]. For the REEs that we analyzed in this study, all of them except Eu have four or more isotopes. Hence, we were able to monitor several pairs of isotope ratios and calculate isotopic anomalies by internal normalization using an exponential fractionation law. The isotopic anomalies recorded in the CAIs were all about two orders of magnitude smaller compared to the stable isotopic fractionation per amu for the same REE. Eu only has two isotopes (^{151}Eu and ^{153}Eu). Thus, the stable isotopic fractionation of Eu cannot be distinguished from isotopic anomalies by monitoring different pairs of isotope ratios. ^{151}Eu has a large thermal neutron capture cross section [9200 barns (b)], but it is much lower than that of ^{157}Gd (255,000 b), which shows cosmogenic effects that would correspond to a shift of 0.05‰/amu if misinterpreted in terms of isotopic fractionation. Both ^{151}Eu and ^{153}Eu are mostly of *r*-process origin. Thus, we can safely assume that Eu isotopic variations are due to stable isotopic fractionation rather than nucleosynthetic anomalies or cosmogenic effects. The fact that Eu isotopic variations correlate with mass-dependent Sr isotopic fractionation (Fig. 2A) supports this view.

Approximately 5% of the matrix cut after U/TEVA chemistry (4% of the whole CAI) was pipetted out and used for analyzing Ti isotopic anomalies. Approximately 5% of the REE matrix cuts were also analyzed for Ti stable isotopic fractionation using the double-spike approach. The isotopic analyses and correction of isotopic anomalies followed (*55*) and (*56*).

Assessment of data accuracy

The data quality of REE isotopic analyses was controlled by measuring the total procedural blank, a terrestrial geostandard, and running replicates. The total procedural blanks for all REEs are less than 0.25 ng, which is negligible compared to the amounts of REEs in the samples. A geostandard (terrestrial basalt BCR-2) was processed with the CAIs. The stable isotopic fractionations normalized to the isotopic standards for all REEs are zero within error bars (typically less than 0.05‰/amu). The three replicates based on the matrix cut of Mo chemistry were found to yield generally consistent results compared to those of the same CAI that have not experienced substantial loss of REEs. The stable isotopic compositions of LREEs in the replicates are shifted to the heavy side by approximately 0.1‰/amu, while HREEs yield the same result within error bars (Table 1). The only exception is Nd in FG-FT-4, which is shifted by 0.4‰/amu. The stable isotopic fractionation of LREEs induced by Mo chemistry (possibly chromatography) is not negligible (~0.1‰/amu) but much less than the natural isotopic fractionations measured in these CAIs (−1 to +1‰/amu for LREEs).

Another piece of evidence demonstrating the accuracy of the data acquired is that our Eu isotopic variations correlate very tightly with Sr isotopic variations measured using a double-spike approach in a different laboratory, using a completely independent chemical procedure and a thermal ionization mass spectrometer (TIMS) for isotopic analysis (*16*).

The data quality of Ti isotope measurements was verified by measuring two geostandards BCR-2 and G-3, which yield values that are consistent with previous measurements (*55*, *57*). The Ti double-spike measurements are also compared to the previous measurement on the same samples using SSB, which are generally consistent but are less precise (table S1).

SUPPLEMENTARY MATERIALS

Supplementary material for this article is available at http://advances.sciencemag.org/cgi/content/full/7/2/eabc2962/DC1

REFERENCES AND NOTES

1. A. G. W. Cameron, The formation of the sun and planets. *Icarus* **1**, 13–69 (1962).
2. L. Grossman, Condensation in the primitive solar nebula. *Geochim. Cosmochim. Acta* **36**, 597–619 (1972).
3. S. Yoneda, L. Grossman, Condensation of CaO-MgO-Al_2O_3-SiO_2 liquids from cosmic gases. *Geochim. Cosmochim. Acta* **59**, 3413–3444 (1995).
4. T. Tanaka, A. Masuda, Rare-earth elements in matrix, inclusions, and chondrules of the Allende meteorite. *Icarus* **19**, 523–530 (1973).
5. B. Mason, S. R. Taylor, Inclusions in the Allende meteorite. *Smithson. Contrib. Earth Sci.* (1982).
6. T. R. Ireland, B. Fegley Jr., The solar system's earliest chemistry: Systematics of refractory inclusions. *Int. Geol. Rev.* **42**, 865–894 (2000).
7. N. Dauphas, A. Pourmand, Thulium anomalies and rare earth element patterns in meteorites and Earth: Nebular fractionation and the nugget effect. *Geochim. Cosmochim. Acta* **163**, 234–261 (2015).
8. J.-A. Barrat, N. Dauphas, P. Gillet, C. Bollinger, J. Etoubleau, A. Bischoff, A. Yamaguchi, Evidence from Tm anomalies for non-CI refractory lithophile element proportions in terrestrial planets and achondrites. *Geochim. Cosmochim. Acta* **176**, 1–17 (2016).
9. F. M. Richter, A. M. Davis, D. S. Ebel, A. Hashimoto, Elemental and isotopic fractionation of Type B calcium-, aluminum-rich inclusions: Experiments, theoretical considerations, and constraints on their thermal evolution. *Geochim. Cosmochim. Acta* **66**, 521–540 (2002).
10. A. Shahar, E. D. Young, Astrophysics of CAI formation as revealed by silicon isotope LA-MC-ICPMS of an igneous CAI. *Earth Planet. Sci. Lett.* **257**, 497–510 (2007).
11. F. M. Richter, P. E. Janney, R. A. Mendybaev, A. M. Davis, M. Wadhwa, Elemental and isotopic fractionation of type B CAI-like liquids by evaporation. *Geochim. Cosmochim. Acta* **71**, 5544–5564 (2007).
12. L. Grossman, S. B. Simon, V. K. Rai, M. H. Thiemens, I. D. Hutcheon, R. W. Williams, A. Galy, T. Ding, A. V. Fedkin, R. N. Clayton, T. K. Mayeda, Primordial compositions of refractory inclusions. *Geochim. Cosmochim. Acta* **72**, 3001–3021 (2008).

13. A. N. Krot, E. R. Scott, M. E. Zolensky, Mineralogical and chemical modification of components in CV3 chondrites: Nebular or asteroidal processing? *Meteoritics* **30**, 748–775 (1995).
14. J. I. Simon, M. K. Jordan, M. J. Tappa, E. A. Schauble, I. E. Kohl, E. D. Young, Calcium and titanium isotope fractionation in refractory inclusions: Tracers of condensation and inheritance in the early solar protoplanetary disk. *Earth Planet. Sci. Lett.* **472**, 277–288 (2017).
15. A. M. Davis, J. Zhang, N. D. Greber, J. Hu, F. L. Tissot, N. Dauphas, Titanium isotopes and rare earth patterns in CAIs: Evidence for thermal processing and gas-dust decoupling in the protoplanetary disk. *Geochim. Cosmochim. Acta* **221**, 275–295 (2018).
16. B. L. A. Charlier, F. L. H. Tissot, N. Dauphas, C. J. N. Wilson, Nucleosynthetic, radiogenic and stable strontium isotopic variations in fine-and coarse-grained refractory inclusions from Allende. *Geochim. Cosmochim. Acta* **265**, 413–430 (2019).
17. K. Lodders, Solar system abundances and condensation temperatures of the elements. *Astrophys. J.* **591**, 1220 (2003).
18. W. V. Boynton, Fractionation in the solar nebula: Condensation of yttrium and the rare earth elements. *Geochim. Cosmochim. Acta* **39**, 569–584 (1975).
19. A. M. Davis, L. Grossman, Condensation and fractionation of rare earths in the solar nebula. *Geochim. Cosmochim. Acta* **43**, 1611–1632 (1979).
20. A. S. Kornacki, B. Fegley Jr., The abundance and relative volatility of refractory trace elements in Allende Ca, Al-rich inclusions: Implications for chemical and physical processes in the solar nebula. *Earth Planet. Sci. Lett.* **79**, 217–234 (1986).
21. G. Pound, J. Hirth, Condensation and evaporation, nucleation and growth kinetics. *Prog. Mater. Sci.* **11**, (1963).
22. F. M. Richter, Timescales determining the degree of kinetic isotope fractionation by evaporation and condensation. *Geochim. Cosmochim. Acta* **68**, 4971–4992 (2004).
23. A. Tsuchiyama, S. Tachibana, T. Takahashi, Evaporation of forsterite in the primordial solar nebula; rates and accompanied isotopic fractionation. *Geochim. Cosmochim. Acta* **63**, 2451–2466 (1999).
24. K. Ozawa, H. Nagahara, Chemical and isotopic fractionations by evaporation and their cosmochemical implications. *Geochim. Cosmochim. Acta* **65**, 2171–2199 (2001).
25. N. Dauphas, F. Poitrasson, C. Burkhardt, H. Kobayashi, K. Kurosawa, Planetary and meteoritic Mg/Si and δ^{30}Si variations inherited from solar nebula chemistry. *Earth Planet. Sci. Lett.* **427**, 236–248 (2015).
26. B. Bourdon, C. Fitoussi, Isotope fractionation during condensation and evaporation during planet formation processes. *ACS Earth Space Chem.* **4**, 1408–1423 (2020).
27. A. V. Fedkin, L. Grossman, F. J. Ciesla, S. B. Simon, Mineralogical and isotopic constraints on chondrule formation from shock wave thermal histories. *Geochim. Cosmochim. Acta* **87**, 81–116 (2012).
28. J. Jouzel, L. Merlivat, Deuterium and oxygen 18 in precipitation: Modeling of the isotopic effects during snow formation. *J. Geophys. Res. Atmos.* **89**, 11749–11757 (1984).
29. T. J. Ireland, F. L. H. Tissot, R. Yokochi, N. Dauphas, Teflon-HPLC: A novel chromatographic system for application to isotope geochemistry and other industries. *Chem. Geol.* **357**, 203–214 (2013).
30. N. Dauphas, F. L. Tissot, R. Yokochi, T. J. Ireland, J. Hu, U.S. Patent 9,884,266 (2018).
31. J. Jiun-San Shen, T. Lee, ^{138}La anomaly in the early solar system. *Astrophys. J. Lett.* **596**, L109 (2003).
32. A. Pourmand, N. Dauphas, T. J. Ireland, A novel extraction chromatography and MC-ICP-MS technique for rapid analysis of REE, Sc and Y: Revising CI-chondrite and Post-Archean Australian Shale (PAAS) abundances. *Chem. Geol.* **291**, 38–54 (2012).
33. E. Albalat, P. Telouk, F. Albarède, Er and Yb isotope fractionation in planetary materials. *Earth Planet. Sci. Lett.* **355**, 39–50 (2012).
34. F. L. H. Tissot, N. Dauphas, L. Grossman, Origin of uranium isotope variations in early solar nebula condensates. *Sci. Adv.* **2**, e1501400 (2016).
35. F. Moynier, A. Bouvier, J. Blichert-Toft, P. Telouk, D. Gasperini, F. Albarede, Europium isotopic variations in Allende CAIs and the nature of mass-dependent fractionation in the solar nebula. *Geochim. Cosmochim. Acta* **70**, 4287–4294 (2006).
36. S. B. Simon, L. Grossman, A. M. Davis, Fassaite composition trends during crystallization of Allende Type B refractory inclusion melts. *Geochim. Cosmochim. Acta* **55**, 2635–2655 (1991).
37. N. Dauphas, M. Y. Hu, E. M. Baker, J. Hu, F. L. H. Tissot, E. E. Alp, M. Roskosz, J. Zhao, W. Bi, J. Liu, J.-F. Lin, N. X. Nie, A. Heard, SciPhon: A data analysis software for nuclear resonant inelastic X-ray scattering with applications to Fe, Kr, Sn, Eu and Dy. *J. Synchrotron Radiat.* **25**, 1581–1599 (2018).
38. S. Gabelnick, G. Reedy, M. Chasanov, Infrared spectra and structure of some matrix-isolated lanthanide and actinide oxides. *J. Chem. Phys.* **60**, 1167–1171 (1974).
39. A. Stracke, H. Palme, M. Gellissen, C. Münker, T. Kleine, K. Birbaum, D. Günther, B. Bourdon, J. Zipfel, Refractory element fractionation in the Allende meteorite: Implications for solar nebula condensation and the chondritic composition of planetary bodies. *Geochim. Cosmochim. Acta* **85**, 114–141 (2012).
40. G. J. MacPherson, A. M. Davis, Refractory inclusions in the prototypical CM chondrite, Mighei. *Geochim. Cosmochim. Acta* **58**, 5599–5625 (1994).
41. H. Palme, F. Wlotzka, K. Nagel, A. El Goresy, An ultra-refractory inclusion from the Ornans carbonaceous chondrite. *Earth Planet. Sci. Lett.* **61**, 1–12 (1982).
42. S. B. Simon, A. M. Davis, L. Grossman, A unique ultrarefractory inclusion from the Murchison meteorite. *Meteorit. Planet. Sci.* **31**, 106–115 (1996).
43. M. Audard, P. Abrahám, M. M. Dunham, J. D. Green, N. Grosso, K. Hamaguchi, J. H. Kastner, A. Kóspál, G. Lodato, M. M. Romanova, Episodic accretion in young stars. *Protostars Planets VI* **387**, (2014).
44. G. Herbig, EX Lupi: History and spectroscopy. *Astron. J.* **133**, 2679 (2007).
45. L. Hartmann, S. J. Kenyon, The FU orionis phenomenon. *Annu. Rev. Astron. Astrophys.* **34**, 207–240 (1996).
46. A. P. Boss, C. M. D. Alexander, M. Podolak, Cosmochemical consequences of particle trajectories during FU Orionis outbursts by the early Sun. *Earth Planet. Sci. Lett.* **345**, 18–26 (2020).
47. A. P. Boss, C. M. D. Alexander, M. Podolak, Evolution of CAI-sized Particles during FU Orionis Outbursts. I. Particle Trajectories in Protoplanetary Disks with Beta Cooling. *The Astrophysical Journal* **901**, 81 (2020).
48. P. Ábrahám, A. Juhász, C. P. Dullemond, Á. Kóspál, R. van Boekel, J. Bouwman, T. Henning, A. Moór, L. Mosoni, A. Sicilia-Aguilar, N. Sipos, Episodic formation of cometary material in the outburst of a young Sun-like star. *Nature* **459**, 224–226 (2009).
49. K. D. McKeegan, J. Aléon, J. Bradley, D. Brownlee, H. Busemann, A. Butterworth, M. Chaussidon, S. Fallon, C. Floss, J. Gilmour, M. Gounelle, G. Graham, Y. Guan, P. R. Heck, P. Hoppe, I. D. Hutcheon, J. Huth, H. Ishii, M. Ito, S. B. Jacobsen, A. Kearsley, L. A. Leshin, M.-C. Liu, I. Lyon, K. Marhas, B. Marty, G. Matrajt, A. Meibom, S. Messenger, S. Mostefaoui, S. Mukhopadhyay, K. Nakamura-Messenger, L. Nittler, R. Palma, R. O. Pepin, D. A. Papanastassiou, F. Robert, D. Schlutter, C. J. Snead, F. J. Stadermann, R. Stroud, P. Tsou, A. Westphal, E. D. Young, K. Ziegler, L. Zimmermann, E. Zinner, Isotopic compositions of cometary matter returned by Stardust. *Science* **314**, 1724–1728 (2006).
50. C. M. Lisse, J. Van Cleve, A. C. Adams, M. F. A'Hearn, Y. R. Fernández, T. L. Farnham, L. Armus, C. J. Grillmair, J. Ingalls, M. J. S. Belton, O. Groussin, L. A. M. Fadden, K. J. Meech, P. H. Schultz, B. C. Clark, L. M. Feaga, J. M. Sunshine, Spitzer spectral observations of the Deep Impact ejecta. *Science* **313**, 635–640 (2006).
51. D. Brownlee, P. Tsou, J. Aléon, C. M. O.'. D. Alexander, T. Araki, S. Bajt, G. A. Baratta, R. Bastien, P. Bland, P. Bleuet, J. Borg, J. P. Bradley, A. Brearley, F. Brenker, S. Brennan, J. C. Bridges, N. D. Browning, J. R. Brucato, E. Bullock, M. J. Burchell, H. Busemann, A. Butterworth, M. Chaussidon, A. Cheuvront, M. Chi, M. J. Cintala, B. C. Clark, S. J. Clemett, G. Cody, L. Colangeli, G. Cooper, P. Cordier, C. Daghlian, Z. Dai, L. D'Hendecourt, Z. Djouadi, G. Dominguez, T. Duxbury, J. P. Dworkin, D. S. Ebel, T. E. Economou, S. Fakra, S. A. J. Fairey, S. Fallon, G. Ferrini, T. Ferroir, H. Fleckenstein, C. Floss, G. Flynn, I. A. Franchi, M. Fries, Z. Gainsforth, J.-P. Gallien, M. Genge, M. K. Gilles, P. Gillet, J. Gilmour, D. P. Glavin, M. Gounelle, M. M. Grady, G. A. Graham, P. G. Grant, S. F. Green, F. Grossemy, L. Grossman, J. N. Grossman, Y. Guan, K. Hagiya, R. Harvey, P. Heck, G. F. Herzog, P. Hoppe, F. Hörz, J. Huth, I. D. Hutcheon, K. Ignatyev, H. Ishii, M. Ito, D. Jacob, C. Jacobsen, S. Jacobsen, S. Jones, D. Joswiak, A. Jurewicz, A. T. Kearsley, L. P. Keller, H. Khodja, A. L. D. Kilcoyne, J. Kissel, A. Krot, F. Langenhorst, A. Lanzirotti, L. Le, L. A. Leshin, J. Leitner, L. Lemelle, H. Leroux, M.-C. Liu, K. Luening, I. Lyon, G. M. Pherson, M. A. Marcus, K. Marhas, B. Marty, G. Matrajt, K. M. Keegan, A. Meibom, V. Mennella, K. Messenger, S. Messenger, T. Mikouchi, S. Mostefaoui, T. Nakamura, T. Nakano, M. Newville, L. R. Nittler, I. Ohnishi, K. Ohsumi, K. Okudaira, D. A. Papanastassiou, R. Palma, M. E. Palumbo, R. O. Pepin, D. Perkins, M. Perronnet, P. Pianetta, W. Rao, F. J. M. Rietmeijer, F. Robert, D. Rost, A. Rotundi, R. Ryan, S. A. Sandford, C. S. Schwandt, T. H. See, D. Schlutter, J. Sheffield-Parker, A. Simionovici, S. Simon, I. Sitnitsky, C. J. Snead, M. K. Spencer, F. J. Stadermann, A. Steele, T. Stephan, R. Stroud, J. Susini, S. R. Sutton, Y. Suzuki, M. Taheri, S. Taylor, N. Teslich, K. Tomeoka, N. Tomioka, A. Toppani, J. M. Trigo-Rodríguez, D. Troadec, A. Tsuchiyama, A. J. Tuzzolino, T. Tyliszczak, K. Uesugi, M. Velbel, J. Vellenga, E. Vicenzi, L. Vincze, J. Warren, I. Weber, M. Weisberg, A. J. Westphal, S. Wirick, D. Wooden, B. Wopenka, P. Wozniakiewicz, I. Wright, H. Yabuta, H. Yano, E. D. Young, R. N. Zare, T. Zega, K. Ziegler, L. Zimmerman, E. Zinner, M. Zolensky, Comet 81P/Wild 2 under a microscope. *Science* **314**, 1711–1716 (2006).
52. M. E. Zolensky, T. J. Zega, H. Yano, S. Wirick, A. J. Westphal, M. K. Weisberg, I. Weber, J. L. Warren, M. A. Velbel, A. Tsuchiyama, P. Tsou, A. Toppani, N. Tomioka, K. Tomeoka, N. Teslich, M. Taheri, J. Susini, R. Stroud, T. Stephan, F. J. Stadermann, C. J. Snead, S. B. Simon, A. Simionovici, T. H. See, F. Robert, F. J. M. Rietmeijer, W. Rao, M. C. Perronnet, D. A. Papanastassiou, K. Okudaira, K. Ohsumi, I. Ohnishi, K. Nakamura-Messenger, T. Nakamura, S. Mostefaoui, T. Mikouchi, A. Meibom, G. Matrajt, M. A. Marcus, H. Leroux, L. Lemelle, L. Le, A. Lanzirotti, F. Langenhorst, A. N. Krot, L. P. Keller, A. T. Kearsley, D. Joswiak, D. Jacob, H. Ishii, R. Harvey, K. Hagiya, L. Grossman, J. N. Grossman, G. A. Graham, M. Gounelle, P. Gillet, M. J. Genge, G. Flynn, T. Ferroir, S. Fallon, D. S. Ebel, Z. R. Dai, P. Cordier, B. Clark, M. Chi, A. L. Butterworth, D. E. Brownlee, J. C. Bridges, S. Brennan, A. Brearley, J. P. Bradley, P. Bleuet, P. A. Bland, R. Bastien, Mineralogy and petrology of comet 81P/Wild 2 nucleus samples. *Science* **314**, 1735–1739 (2006).

53. S. Simon, A. Davis, L. Grossman, Origin of compact type A refractory inclusions from CV3 carbonaceous chondrites. *Geochim. Cosmochim. Acta* **63**, 1233–1248 (1999).
54. Q. R. Shollenberger, J. Render, G. A. Brennecka, Er, Yb, and Hf isotopic compositions of refractory inclusions: An integrated isotopic fingerprint of the solar system's earliest reservoir. *Earth Planet. Sci. Lett.* **495**, 12–23 (2018).
55. N. D. Greber, N. Dauphas, I. S. Puchtel, B. A. Hofmann, N. T. Arndt, Titanium stable isotopic variations in chondrites, achondrites and lunar rocks. *Geochim. Cosmochim. Acta* **213**, 534–552 (2017).
56. J. Y. Hu, N. Dauphas, Double-spike data reduction in the presence of isotopic anomalies. *J. Anal. At. Spectrom.* **32**, 2024–2033 (2017).
57. M.-A. Millet, N. Dauphas, Ultra-precise titanium stable isotope measurements by double-spike high resolution MC-ICP-MS. *J. Anal. At. Spectrom.* **29**, 1444–1458 (2014).
58. T. R. Ireland, Correlated morphological, chemical, and isotopic characteristics of hibonites from the Murchison carbonaceous chondrite. *Geochim. Cosmochim. Acta* **52**, 2827–2839 (1988).
59. G. A. Brennecka, S. Weyer, M. Wadhwa, P. E. Janney, J. Zipfel, A. D. Anbar, $^{238}U/^{235}U$ variations in meteorites: Extant ^{247}Cm and implications for Pb-Pb dating. *Science* **327**, 449–451 (2010).
60. H. Tang, M.-C. Liu, K. D. McKeegan, F. L. Tissot, N. Dauphas, In situ isotopic studies of the U-depleted Allende CAI Curious Marie: Pre-accretionary alteration and the co-existence of ^{26}Al and ^{36}Cl in the early solar nebula. *Geochim. Cosmochim. Acta* **207**, 1–18 (2017).

Acknowledgments: CAI samples were provided by P. R. Heck and the Robert A. Pritzker Center for Meteoritics and Polar Studies at the Field Museum (FG-FT-3, 4, 6, 7, 8, 9, and 10) and S. Simon (TS32) (see full catalog numbers in Table 1). Discussions with F. M. Richter, P. R. Heck, N. X. Nie, C. Chen, H. Zeng, S. M. Aarons, and A. W. Heard were greatly appreciated. We are grateful to H. Palme and an anonymous reviewer for thorough and constructive reviews, which greatly improved the quality of the manuscript. **Funding:** This work was supported by NASA grants NNX17AE86G, NNX17AE87G, 80NSSC17K0744, and 80NSSC20K0821; NSF grant EAR-2001098 to N.D.; and NASA grant 80NSSC17K0251 to A.M.D. **Author contributions:** J.Y.H., N.D., and F.L.H.T. conceived the study; F.L.H.T. and L.G. selected the samples in a previous study; F.L.H.T. characterized, extracted, and digested the samples; J.Y.H. established the measurement protocol, carried out the isotopic analyses of REEs, did the modeling, and wrote a first draft of the manuscript under the guidance of N.D.; Z.Z. and J.Y.H. carried out the isotopic analyses of Ti; A.M.D. helped with thermodynamic modeling; F.J.C. provided some input on the possible astrophysical setting for CAI formation; N.D., F.L.H.T., R.Y., T.J.I., and J.Y.H. developed the FPLC system; B.L.A.C. helped with comparison of the data with previous Sr isotopic results; N.D., M.R., E.E.A., M.Y.H., and J.Z. helped with interpretation of previously published Eu NRIXS data. All authors contributed to data interpretation and writing of the manuscript. **Competing interests:** N.D., F.L.H.T., R.Y., T.J.I., and J.Y.H. are inventors on a patent related to this work filed by Orlab Chromatography LLC (no. US9884266B2, filed on 8 July 2014, published on 8 January 2015). The authors declare no other competing interests. **Data and materials availability:** The OL-REE series of isotope standards used in this study are stored at the Origins Laboratory, The University of Chicago and are available upon request from J.Y.H. or N.D. All data needed to evaluate the conclusions in the paper are present in the paper and/or the Supplementary Materials. Additional data related to this paper may be requested from the authors.

Submitted 16 April 2020
Accepted 16 November 2020
Published 6 January 2021
10.1126/sciadv.abc2962

Citation: J. Y. Hu, N. Dauphas, F. L. H. Tissot, R. Yokochi, T. J. Ireland, Z. Zhang, A. M. Davis, F. J. Ciesla, L. Grossman, B. L. A. Charlier, M. Roskosz, E. E. Alp, M. Y. Hu, J. Zhao, Heating events in the nascent solar system recorded by rare earth element isotopic fractionation in refractory inclusions. *Sci. Adv.* **7**, eabc2962 (2021).

ScienceAdvances

Heating events in the nascent solar system recorded by rare earth element isotopic fractionation in refractory inclusions

J. Y. HuN. DauphasF. L. H. TissotR. YokochiT. J. IrelandZ. ZhangA. M. DavisF. J. CieslaL. GrossmanB. L. A. CharlierM. RoskoszE. E. AlpM. Y. HuJ. Zhao

Sci. Adv., 7 (2), eabc2962. • DOI: 10.1126/sciadv.abc2962

Science Advances (ISSN) is published by the American Association for the Advancement of Science. 1200 New York Avenue NW, Washington, DC 20005. The title *Science Advances* is a registered trademark of AAAS.

Science Advances
AAAS

advances.sciencemag.org/cgi/content/full/7/2/eabc2962/DC1

Supplementary Materials for

Heating events in the nascent solar system recorded by rare earth element isotopic fractionation in refractory inclusions

J. Y. Hu*, N. Dauphas, F. L. H. Tissot, R. Yokochi, T. J. Ireland, Z. Zhang, A. M. Davis, F. J. Ciesla, L. Grossman, B. L. A. Charlier, M. Roskosz, E. E. Alp, M. Y. Hu, J. Zhao

*Corresponding author. Email: jingya@uchicago.edu

Published 6 January 2021, *Sci. Adv.* **7**, eabc2962 (2021)
DOI: 10.1126/sciadv.abc2962

This PDF file includes:

Supplementary Online Materials

Modeling of Stable Isotopic Fractionation Induced by Evaporation and Condensation

1. Speciation of REEs during Evaporation and Condensation

In this section, we calculate the vapor pressures of the different species of a REE in equilibrium with hibonite. Hibonite is a highly refractory mineral that has been implicated in establishing the REE abundance pattern of group II CAIs (*15, 19*). According to equilibrium thermodynamics (*15, 19*), REEs can exist in the form of 6 species under solar nebula conditions, where 3 species are present in gaseous forms (noted as $M^0{}_{(g)}$, $M^{2+}O_{(g)}$, $M^{4+}O_{2(g)}$) and the other 3 species substitute for Ca in solid solution in refractory minerals such as hibonite and perovskite ($M^{2+}O_{(s)}$, $M^{3+}O_{1.5(s)}$, $M^{4+}O_{2(s)}$). At equilibrium, the partial pressures and molar densities of different species are related to each other through the following equilibria:

$$M_{(g)} + O_{(g)} = MO_{(g)},$$

$$K_1 = \frac{P_{MO}}{P_M P_O}, \tag{S1}$$

$$2MO_{1.5(s)} = 2M_{(g)} + 3O_{(g)},$$

$$K_2 = \frac{{P_M}^2 {P_O}^3}{\left(\chi_{MO_{1.5}} n_{MO_{1.5}}/n_{Ca}\right)^2}, \tag{S2}$$

$$M_{(g)} + 2O_{(g)} = MO_{2(g)},$$

$$K_3 = \frac{P_{MO_2}}{P_M {P_O}^2}, \tag{S3}$$

$$MO_{2(s)} = M_{(g)} + 2O_{(g)},$$

$$K_4 = \frac{P_M {P_O}^2}{\chi_{MO_2} n_{MO_2}/n_{Ca}}, \tag{S4}$$

$$MO_{(s)} = M_{(g)} + O_{(g)},$$

$$K_5 = \frac{P_M P_O}{\chi_{MO} n_{MO}/n_{Ca}}, \tag{S5}$$

where K_1–K_5 are the equilibrium constants of the chemical reactions, P_ℓ, χ_ℓ, and n_ℓ, are, respectively, the partial pressures, activity coefficients, and solid molar densities of the REE considered (number of moles of M, MO, MO_2), P_O is the partial pressure of atomic oxygen (the value of P_O for solar nebula conditions is provided in (*3, 15*)), and n_{Ca} is the solid molar

density of Ca (condensed REEs are expected to substitute for Ca in refractory minerals). One can rearrange the equations above and write P_M, P_{MO}, P_{MO_2}, n_{MO_2}, n_{MO} as functions of P_O, K_1 to K_5, χ_M, χ_{MO}, χ_{MO_2}, $n_{MO_{1.5}}$ and n_{Ca},

$$P_M = \sqrt{K_2}\frac{1}{{P_O}^{1.5}}\frac{\chi_{MO_{1.5}}}{n_{Ca}}n_{MO_{1.5}}, \tag{S6}$$

$$P_{MO} = K_1\sqrt{K_2}\frac{1}{\sqrt{P_O}}\frac{\chi_{MO_{1.5}}}{n_{Ca}}n_{MO_{1.5}}, \tag{S7}$$

$$P_{MO_2} = \sqrt{K_2}K_3\sqrt{P_O}\frac{\chi_{MO_{1.5}}}{n_{Ca}}n_{MO_{1.5}}, \tag{S8}$$

$$n_{MO_2} = \frac{\sqrt{K_2}}{K_4}\sqrt{P_O}\frac{\chi_{MO_{1.5}}}{\chi_{MO_2}}n_{MO_{1.5}}, \tag{S9}$$

$$n_{MO} = \frac{\sqrt{K_2}}{K_5}\frac{1}{\sqrt{P_O}}\frac{\chi_{MO_{1.5}}}{\chi_{MO}}n_{MO_{1.5}}. \tag{S10}$$

The total molar density of a given condensed REE is given by the sum of 3 solid species,

$$n_{Mtot} = n_{MO} + n_{MO_{1.5}} + n_{MO_2}. \tag{S11}$$

Accordingly, one can write $n_{MO_{1.5}}$ as a function of n_{Mtot} using Eqs. S9–S11,

$$n_{MO_{1.5}} = \frac{n_{Mtot}}{1+\frac{\sqrt{K_2}}{K_5}\frac{1}{\sqrt{P_O}}\frac{\chi_{MO_{1.5}}}{\chi_{MO}}+\frac{\sqrt{K_2}}{K_4}\sqrt{P_O}\frac{\chi_{MO_{1.5}}}{\chi_{MO_2}}}. \tag{S12}$$

In the same manner, the partial pressures of $M_{(g)}$, $MO_{(g)}$ and $MO_{2\,(g)}$ can be written as a function of n_{Mtot} and P_{Mtot},

$$P_M = \frac{1}{P_O}\frac{1}{\frac{1}{K_5\chi_{MO}}+\frac{\sqrt{P_O}}{\sqrt{K_2}\chi_{MO_{1.5}}}+\frac{P_O}{K_4\chi_{MO_2}}}\frac{n_{Mtot}}{n_{Ca}}, \tag{S13}$$

$$P_{MO} = K_1\frac{1}{\frac{1}{K_5\chi_{MO}}+\frac{\sqrt{P_O}}{\sqrt{K_2}\chi_{MO_{1.5}}}+\frac{P_O}{K_4\chi_{MO_2}}}\frac{n_{Mtot}}{n_{Ca}}, \tag{S14}$$

$$P_{MO_2} = K_3P_O\frac{1}{\frac{1}{K_5\chi_{MO}}+\frac{\sqrt{P_O}}{\sqrt{K_2}\chi_{MO_{1.5}}}+\frac{P_O}{K_4\chi_{MO_2}}}\frac{n_{Mtot}}{n_{Ca}}, \tag{S15}$$

$$P_M = \frac{1/P_O}{1/P_O+K_1+K_3P_O}P_{Mtot} = x_MP_{Mtot}, \tag{S16}$$

$$P_{MO} = \frac{K_1}{1/P_O+K_1+K_3P_O}P_{Mtot} = x_{MO}P_{Mtot}, \tag{S17}$$

$$P_{MO_2} = \frac{K_3P_O}{1/P_O+K_1+K_3P_O}P_{Mtot} = x_{MO_2}P_{Mtot}. \tag{S18}$$

where x_ℓ are the mole fraction of the various gas species. We also have for the total vapor pressure of a REE,

$$P_{Mtot} = \frac{1/P_O + K_1 + K_3 P_O}{\frac{1}{K_5 \chi_{MO}} + \frac{\sqrt{P_O}}{\sqrt{K_2}\chi_{MO_{1.5}}} + \frac{P_O}{K_4 \chi_{MO_2}}} \frac{n_{Mtot}}{n_{Ca}} = \kappa \frac{n_{Mtot}}{n_{Ca}}, \quad \text{(S19)}$$

where κ is a factor that relates the equilibrium vapor pressure to the concentration (molar density) in the solid. Equations S13–S15 can be used to calculate the equilibrium pressures of gaseous species if the molar density of the REEs in solid, temperature, thermodynamic constants, and oxygen partial pressure are known.

2. REE Abundance and Stable Isotopic Fractionation during Evaporation

In this section, our goal is to develop a quantitative model of the depletions and stable isotopic fractionations of all REEs during evaporation. Most REEs are thought to have been quantitative evaporated during the first stage of evaporation envisioned here. The only REEs that were not quantitatively evaporated are the most refractory ones, notably Gd and Dy. In fine-grained CAIs, we find that these REEs are highly depleted relative to moderately refractory REEs and have light isotopic compositions. This is more readily explained if the signature of group II REE patterns in CAIs were inherited from an episode of evaporation, whereby the most refractory REEs were only partially evaporated in an undersaturated medium, resulting in their light isotope enrichment in the gas phase, which latter partially re-condensed to form CAIs with group II REE patterns. For this first evaporation stage, we are therefore primarily interested in the isotopic composition of the vapor. Our primary aim here is to use the isotopic composition of the most refractory REEs to put constraints on the rate of heating and duration of the evaporation episode. According to the Hertz-Knudsen equation, the net flux for each REE i during evaporation is given by,

$$J_i = \sum_\ell \frac{\gamma_{\ell,i}\left(P_{eq,\ell,i} - P_{\ell,i}\right)}{\sqrt{2\pi m_{\ell,i} RT}}, \quad \text{(S20)}$$

where ℓ enumerates the gaseous species $M_{(g)}$, $MO_{(g)}$ and $MO_{2(g)}$, $\gamma_{\ell,i}$ and $m_{\ell,i}$ are the condensation/evaporation coefficients and masses of the corresponding species, R is the gas constant, $P_{\ell,i}$ and $P_{eq,\ell,i}$ are the partial and equilibrium vapor pressures, respectively. The equilibrium vapor pressure $P_{eq,\ell,i}$ in Eq. S20 is the partial pressure that is in equilibrium with the condensate at temperature T, as is derived in Eqs. S13–S15.

We consider a model where refractory inclusions of similar sizes and evenly distributed in space are evaporated. This model is similar to those applied to closed-system condensation/evaporation and chondrule formation (*22-24, 26, 27*). Under these conditions, we do not need to track a whole ensemble of refractory inclusions and can only consider a single CAI of radius r surrounded by a parcel of gas of finite volume $V_g = 4\pi\mathcal{R}^3/3$ with no-flux boundary conditions at the boundaries ($\mathcal{R}$ is the radius of the system inclusion+gas, which is much larger than the radius r of the inclusion itself). From a practical point of view, this is equivalent to considering a local closed-system. We assume that the driver for evaporation is heating, with the temperature increasing linearly with time, $T(t) = T_0 + \Phi t$, where T_0 is the initial temperature, Φ is the heating rate, and t is the time elapsed since the onset of heating. If inclusion and gas form a closed system, the evaporation flux must be balanced by a change in the vapor pressure $dP_{\ell,i}$ (we use the ideal gas law here),

$$\sum_\ell \frac{4\pi\mathcal{R}^3 dP_{\ell,i}}{3RT} = \sum_\ell \frac{\gamma_{\ell,i}\left(P_{eq,\ell,i}-P_{\ell,i}\right)}{\sqrt{2\pi m_{\ell,i}RT}} 4\pi r^2 dt. \quad \text{(S21)}$$

Different gas species can be lost at different rates depending on their masses and evaporation coefficients, so the speciation of the vaporized gas does not necessarily reflect equilibrium vapor pressures. We assume that once in the gas, the different gas species have the opportunity to re-equilibrate and we have,

$$P_{\ell,i} = \frac{P_{eq,\ell,i}}{P_{eq,i}} P_i. \quad \text{(S22)}$$

with $P_i = \sum_\ell P_{\ell,i}$ and $P_{eq,i} = \sum_\ell P_{eq,\ell,i}$. Using Eqs. S21 and S16-S18 ($P_{eq,\ell,i} = x_{\ell,i}P_{eq,i}$), we can rewrite Eq. S21 as,

$$\frac{dP_i}{dt} = 3\Upsilon_i\left(P_{eq,i} - P_i\right)\sqrt{\frac{RT}{2\pi}}\frac{r^2}{\mathcal{R}^3}, \quad \text{(S23)}$$

with $\Upsilon_i = \sum_\ell \gamma_{\ell,i} x_{\ell,i}/\sqrt{m_{\ell,i}}$. P_i is related to the total number of moles of i in the gas $\eta_{g,i}$ by the ideal gas law, and $P_{eq,i}$ is related to the total number of moles of i in the solid $\eta_{s,i}$ through Eq. S19. We thus have,

$$\frac{d\eta_{g,i}}{dt} = 3\Upsilon_i\left(\kappa_i \frac{4\pi\mathcal{R}^3\eta_{s,i}}{3RT\eta_{s,Ca}} - \eta_{g,i}\right)\sqrt{\frac{RT}{2\pi}}\frac{r^2}{\mathcal{R}^3}, \quad \text{(S24)}$$

where $\eta_{s,Ca}$ are the total number of Ca substitution sites in the solid. We consider that before vapor dissipation, gas and solid form a closed system, so we have $\eta_{g,i} + \eta_{s,i} = \eta_{tot,i}$ with $\eta_{tot,i}$ a constant. If we introduce $f_{g,i} = \eta_{g,i}/\eta_{tot,i}$ the fraction of i that has been evaporated, we have,

$$\frac{df_{g,i}}{dt} = 3\Upsilon_i\left[\kappa_i \frac{4\pi\mathcal{R}^3\,(1-f_{g,i})}{3RT\eta_{s,Ca}} - f_{g,i}\right]\sqrt{\frac{RT}{2\pi}}\frac{r^2}{\mathcal{R}^3}. \quad \text{(S25)}$$

If we assume that the precursor is made of hibonite, one can calculate the number of moles of Ca sites using the density ρ_{hib} and molar mass m_{hib} of hibonite,

$$\eta_{s,Ca} = \rho_{hib}\frac{4}{3}\pi r^3/m_{hib}. \quad \text{(S26)}$$

We therefore have for Eq. S25,

$$\frac{df_{g,i}}{dt} = \Upsilon_i\left[\frac{3m_{hib}\kappa_i}{\sqrt{2\pi RT}\rho_{hib}r}(1-f_{g,i}) - 3\sqrt{\frac{RT}{2\pi}}\frac{r^2}{\mathcal{R}^3}f_{g,i}\right]. \quad \text{(S27)}$$

If we change the differentiation variable from t to T and write $T = T(t)$, Eq. S27 becomes,

$$\frac{df_{g,i}}{dT} = \frac{\Upsilon_i}{\dot{T}}\left[\frac{3m_{hib}\kappa_i}{\sqrt{2\pi RT}\rho_{hib}r}(1-f_{g,i}) - 3\sqrt{\frac{RT}{2\pi}}\frac{r^2}{\mathcal{R}^3}f_{g,i}\right]. \quad \text{(S28)}$$

Assuming that the temperature increasing linearly with time, $T(t) = T_0 + \Phi t$, $\dot{T} = \Phi$. Equation S28 takes the form,

$$\frac{df_{g,i}}{dT} = \frac{\Upsilon_i}{\Phi}\left[\frac{3m_{hib}\kappa_i}{\sqrt{2\pi RT}\rho_{hib}r}(1 - f_{g,i}) - 3\sqrt{\frac{RT}{2\pi}}\frac{r^2}{\mathcal{R}^3}f_{g,i}\right]. \quad \text{(S29)}$$

Equation S29 can be integrated starting at a low temperature with the initial condition $f_{g,i} = 0\ at\ T = T_0$, and we get the fraction of element i evaporated,

$$f_{g,i} = e^{-\int_1^T \frac{\Upsilon_i}{\Phi}\left(\frac{3m_{hib}\kappa_i}{\sqrt{2\pi RT}\rho_{hib}r} + 3\sqrt{\frac{RT}{2\pi\mathcal{R}^3}}r^2\right)dT} \int_{T_0}^{T} \frac{\Upsilon_i}{\Phi}\frac{3m_{hib}\kappa_i}{\sqrt{2\pi RT}\rho_{hib}r} e^{\int_1^T \frac{\Upsilon_i}{\Phi}\left(\frac{3m_{hib}\kappa_i}{\sqrt{2\pi RT}\rho_{hib}r} + 3\sqrt{\frac{RT}{2\pi\mathcal{R}^3}}r^2\right)dT} dT. \quad \text{(S30)}$$

The isotopic composition was calculated by applying Eq. S30 to different isotopes of the REEs using $\delta_{g,i,2/1} = 1000\ln(f_{g,i,2}/f_{g,i,1})/(m_{i,2} - m_{i,1})$, where $m_{i,1}$ and $m_{i,2}$ are the molecular mass of isotope 1 and 2 of REE i respectively. The parameters that can differ in Eq. S29 between two isotopes are Υ_i and κ_i, where Υ_i is a function of $\gamma_{\ell,i}$, $x_{\ell,i}$ and $m_{\ell,i}$. We only vary $m_{\ell,i}$ and keep the other parameters constant. The fraction and the isotopic fractionation of the element evaporated are both functions of the heating rate and final temperature (duration) of the evaporation episode. We can therefore constrain the heating rate and duration from the depletion of the element considered relative to Sm (fraction evaporated), and the isotopic composition of the CAIs with group II REE patterns (corresponding to the composition of the gas except for Eu and Yb).

For numerical calculations, the precursor is assumed to be a sphere with radius *r* of 40 μm, a typical size for hibonite inclusions in Murchison (70 to 150 μm in their longest dimensions; (*58*)). The ambient pressure during evaporation is set to 10^{-3} bar H_2. We assume that the system has solar bulk composition. To calculate the whole system radius, we use $\aleph_{Ca}$ the number of moles of Ca condensed per unit volume of the system solid+gas, which is from an Excel spreadsheet provided as supplementary online material in (*15*). Indeed, we have $\aleph_{Ca}4\pi\mathcal{R}^3/3 = n_{Ca}4\pi r^3/3$ and $\mathcal{R} = r(n_{Ca}/\aleph_{Ca})^{1/3}$ where $n_{Ca} = 5.42$ mol/L is the Ca molar density of hibonite. The density ρ_{hib} and molar mass m_{hib} of the host mineral hibonite are 3.84 g/cm^3 and 708.8 g/mol, respectively. The radius of the system inclusion+gas $\mathcal{R}$ used is accordingly ~5 m. The sticking coefficients $\gamma_{\ell,i}$ of the REEs are not known and set to 0.1 based on the range of the sticking coefficients of Mg and SiO in melt of CAI composition (*9*). The oxygen fugacity P_O is from a previous condensation calculation (*3*) and is provided in an Excel spreadsheet in the Supplementary Online materials of (*15*). The molar masses $m_{M,i}$ of REEs used for calculation in g/mol are 138.91 (La), 140.12 (Ce), 140.91 (Pr), 144.24 (Nd), 150.36 (Sm), 151.96 (Eu), 157.25 (Gd), 158.93 (Tb), 162.50 (Dy), 164.93 (Ho), 167.26 (Er), 168.93 (Tm), 173.04 (Yb), 174.97 (Lu), respectively. Other thermodynamic data for the REEs, such as the Gibbs free energy and activity coefficients ($\chi_{\ell,i}$) can be found in the supplementary material of (*15*). The choice of the precursor size and thermodynamic data have little effect on the interpretation of the thermal event given the great difference in terms of timescales for the astrophysical events that are considered.

3. REE Abundance and Stable Isotopic Fractionation during Condensation

We envision a two-step process for establishing group II REE pattern. In the first step, all REEs except the most refractory ones are quantitatively evaporated (Sect. 2). This means that Eu and Yb are in the vapor. In the second step, the vapor thus produced is partially

condensed. Moderately refractory REEs are uniformly enriched in CAIs and display subdued stable isotopic fractionations. We therefore expect that during this condensation step, only the least refractory Eu and Yb remain in the vapor, while other REEs are quantitatively condensed.

Eu and Yb are depleted in CAIs with group II REE patterns but show rather subdued isotopic fractionations. This observation can be explained if condensation occurred under near-equilibrium conditions. Cooling must have been protracted to prevent the buildup of large supersaturation, thereby limiting the extent of kinetic isotopic fractionation. Indeed, if cooling had been fast, the equilibrium vapor pressure would have decreased rapidly and the rate of condensation of gas atoms would not have been sufficient to keep up with this decrease. Large kinetic isotope effects associated with supersaturation would have developed, which is not seen for Eu and Yb. Below, we present a model to translate our measurements into a quantitative assessment of cooling rates and timescales. We model condensation assuming closed-system behavior (also see (*22, 26*)) until gas dissipation.

We assume that the CAIs are of equal sizes and evenly distributed in space. We assume that during cooling and condensation, gas and CAI form a closed system. Elements condense following linear cooling until a time/temperature when vapor is dissipated. If the CAIs are all identical and evenly distributed, we do not need to track a whole ensemble of CAIs and can instead only consider a single CAI of radius r surrounded by a parcel of gas of finite volume $V_g = 4\pi\mathcal{R}^3/3$ with no-flux boundary conditions at the boundaries, which from a practical point of view is equivalent to considering a local closed-system. The decrease in the amount of element i in the gas residue is related to the condensation net flux,

$$-\sum_\ell \frac{4\pi\mathcal{R}^3 dP_{\ell,i}}{3RT} = \sum_\ell \frac{\gamma_{\ell,i}\left(P_{\ell,i}-P_{eq,\ell,i}\right)}{\sqrt{2\pi m_{\ell,i}RT}} 4\pi r^2 dt. \quad \text{(S31)}$$

The steps in the derivation of the differential equation governing condensation are similar to those used to derive Eq. S27 and will not be repeated here,

$$\frac{df_{s,i}}{dt} = \Upsilon_i \left[3\sqrt{\frac{RT}{2\pi}}\frac{r^2}{\mathcal{R}^3}\left(1-f_{s,i}\right) - \frac{3m_{hib}\kappa_i}{\sqrt{2\pi RT}\rho_{hib}r} f_{s,i}\right]. \quad \text{(S32)}$$

Changing the differentiation variable from t to T, and writing $T = T(t)$, we have,

$$\frac{df_{s,i}}{dT} = \frac{\Upsilon_i}{\dot{T}} \left[3\sqrt{\frac{RT}{2\pi}}\frac{r^2}{\mathcal{R}^3}\left(1-f_{s,i}\right) - \frac{3m_{hib}\kappa_i}{\sqrt{2\pi RT}\rho_{hib}r} f_{s,i}\right]. \quad \text{(S33)}$$

If we parameterize cooling as $T(t) = T_0 + \Phi t$, like in the evaporation section, with T_0 the starting temperature and Φ (a negative number) the cooling rate, we can write an equation similar to Eq. S29 for the solid condensate,

$$\frac{df_{s,i}}{dT} = \frac{\Upsilon_i}{\Phi} \left[3\sqrt{\frac{RT}{2\pi}}\frac{r^2}{\mathcal{R}^3}\left(1-f_{s,i}\right) - \frac{3m_{hib}\kappa_i}{\sqrt{2\pi RT}\rho_{hib}r} f_{s,i}\right]. \quad \text{(S34)}$$

Integrating Eq. S29 or S34 starting at a high temperature with the initial condition $f_{s,i} = 0\ at\ T = T_0$, we can calculate the fraction of i that has condensed as a function of temperature,

$$f_{s,i} = e^{-\int_1^T \frac{\Upsilon_i}{\Phi}\left(\frac{3m_{hib}\kappa_i}{\sqrt{2\pi RT}\rho_{hib}r}+3\sqrt{\frac{RT}{2\pi\mathcal{R}^3}}r^2\right)dT} \int_{T_0}^{T} 3\frac{\Upsilon_i}{\Phi}\sqrt{\frac{RT}{2\pi}}\frac{r^2}{\mathcal{R}^3} e^{\int_1^T \frac{\Upsilon_i}{\Phi}\left(\frac{3m_{hib}\kappa_i}{\sqrt{2\pi RT}\rho_{hib}r}+3\sqrt{\frac{RT}{2\pi\mathcal{R}^3}}r^2\right)dT} dT. \quad \text{(S35)}$$

The numerical values used in the condensation calculation are very similar to those used during evaporation. The free parameters are the heating rate and duration of the evaporation, which can be constrained by combining measurements of the depletion and isotopic fractionation of Eu and Yb. In our calculation, we assume a starting temperature of 1700 K, at which hibonite is thought to have started condensing but REEs are still mostly in the gas phase.

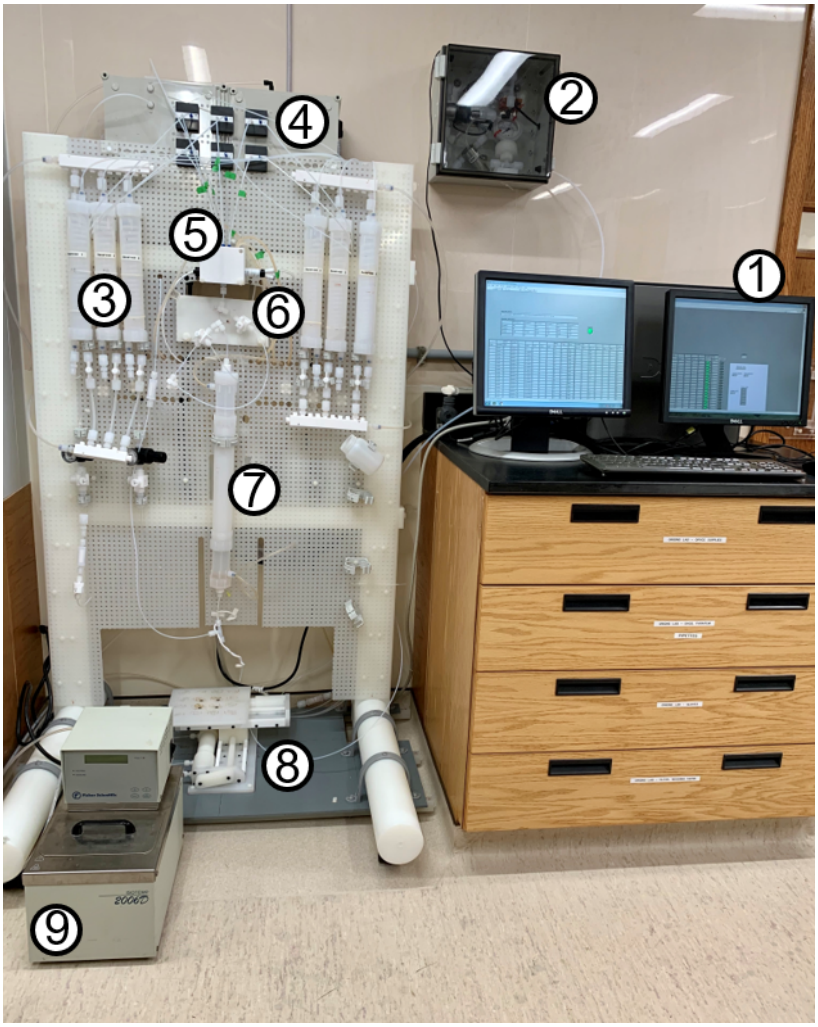

Fig. S1. FPLC system. 1. Control station with Labview software. **2.** Gas switch. If the pressure of the building-supplied high-purity N_2 from a nitrogen generator goes below 60 PSI, the gas source switches to a cylinder of compressed N_2. **3.** Temperature-controlled water/reagent reservoirs. **4.** Electronic bay and pneumatic PTFE positive displacement diaphragm metering pumps. The electronics are within a positively pressurized box to avoid contact with acid fumes. **5.** Temperature-controlled mixing chamber. Reagents introduced by the metering pumps are mixed using a magnetic stirring bar controlled by an external pneumatic micromotor. **6.** Sample introduction loop. **7.** Chromatography column. The column is made of a fine PTFE tube (1.6 mm inner diameter and 70 cm length here) that runs through a Teflon jacket where water is flowing at a set temperature. **8.** Stage. A 16-position pneumatic all-plastic stage is used to dispense the elution cuts in different beakers. **9.** Heating circulating water bath. Many modifications were made after (*29*), notably the conversion to all-pneumatic actuation (including fluoropolymer metering pumps), addition of a sample introduction loop, migration of the electronics to a positively-pressurized box, and development and implementation of a pneumatically-actuated plastic-made 16-position stage (*30*). Photo credit: Justin Hu, The University of Chicago.

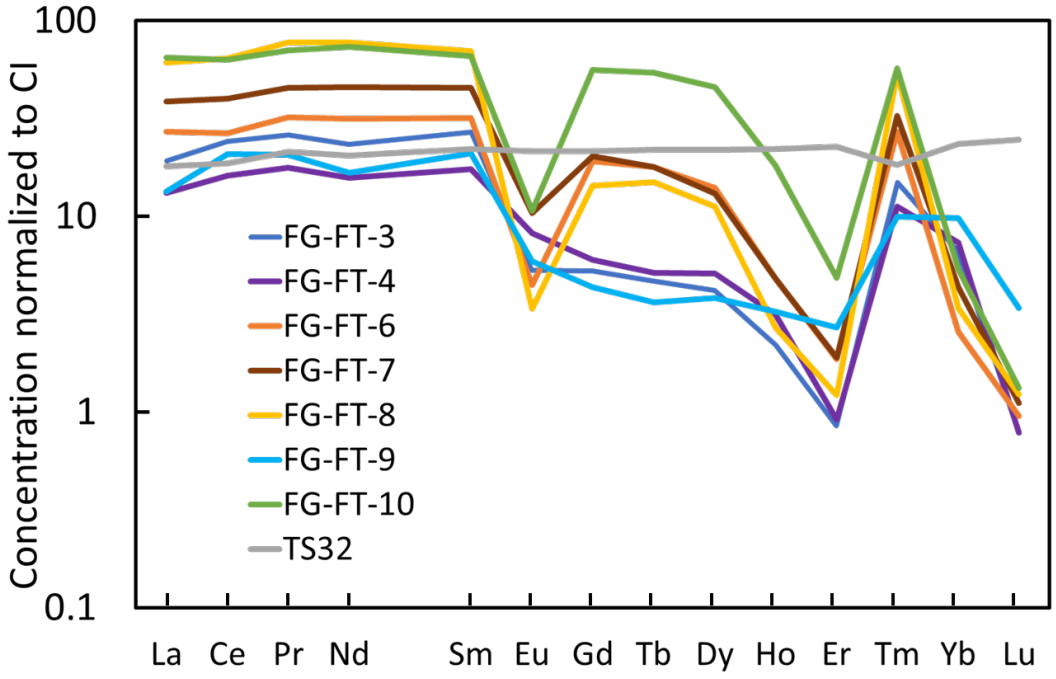

Fig. S2. REE abundance patterns of the 8 CAIs (7 with group II REE patterns) studied here, in order of atomic number (*15, 34*)**.**

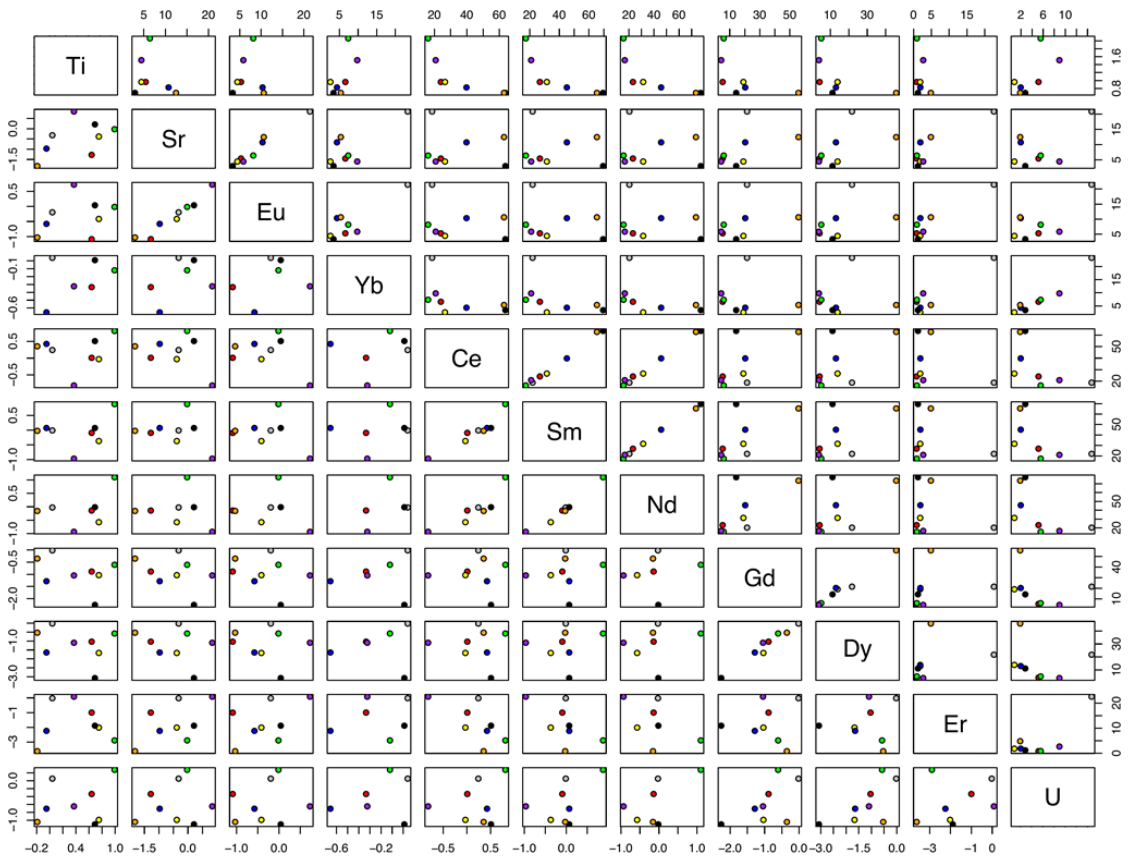

Fig. S3. Scatter plot matrix of 7 group II CAIs. The top right plots are correlations of the abundances normalized to CI chondrites, while the bottom left plots are the correlations of the stable isotopic fractionations (‰/amu). Circles in grey, red, green, yellow, blue, black, purple and orange correspond to CAIs TS32, FG-FT-3, 4, 6, 7, 8, 9 and 10, respectively. Note that in this diagram, none of the plots displays enrichment factor *vs*. isotopic composition (or vice versa).

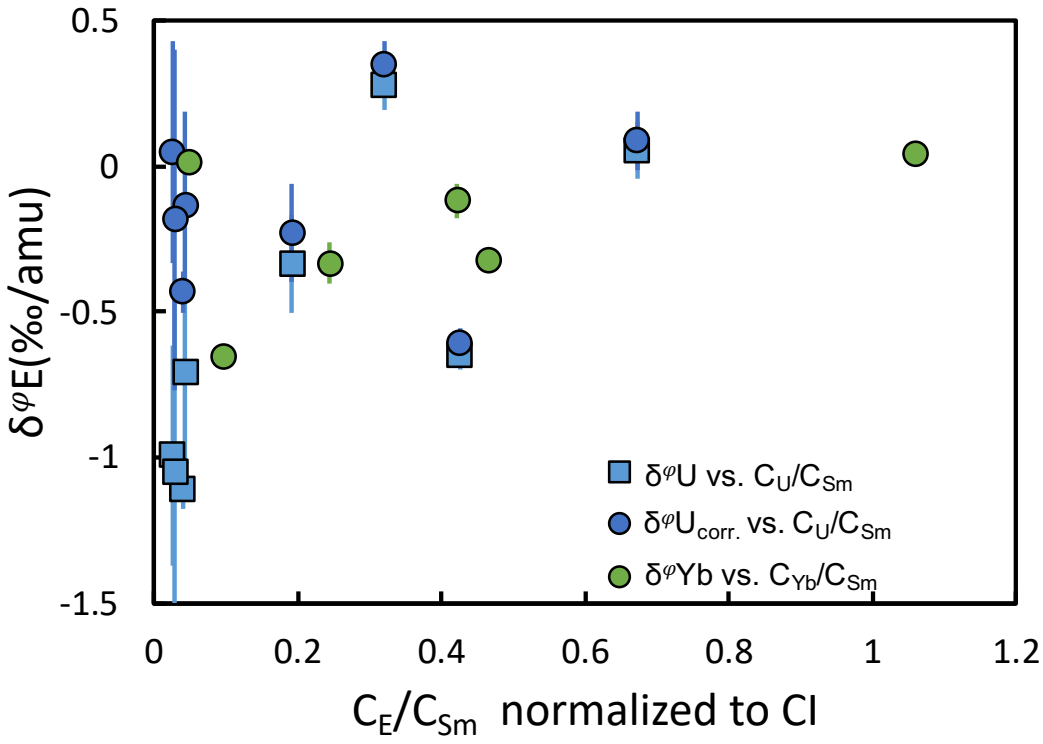

Fig. S4. Yb (green) and U (blue) isotopic compositions plotted as a function of their depletions relative to Sm in CAIs. The Yb isotopic data are from Table 1, while the U isotopic data are from (*34*). The blue-filled squares are raw U isotopic data (δ^{φ}U), while the blue filled-circles ($\delta^{\varphi}U_{corr.}$) have been corrected for decay of ^{247}Cm ($t_{1/2}$ = 15.6 My) using an initial $^{247}Cm/^{235}U$ ratio of 7.0×10^{-5} (*34, 59, 60*) and using the Nd/U ratio as a measure of the fractionation of the Cm/U ratio. As shown, the CAIs show no correlation between δ^{φ}Yb and δ^{φ}U, despite the broad logarithmic correlation of their concentrations (*34*). It is worth noting that the correlation in (*34*) is visible in logarithmic scale but the scatter in the data points around the 1:1 line spans an order of magnitude. The lack of correlation between δ^{φ}Yb and δ^{φ}U could be due to their distinct volatilities or due to U mobilization during aqueous alteration of fine-grained CAIs (*34*).

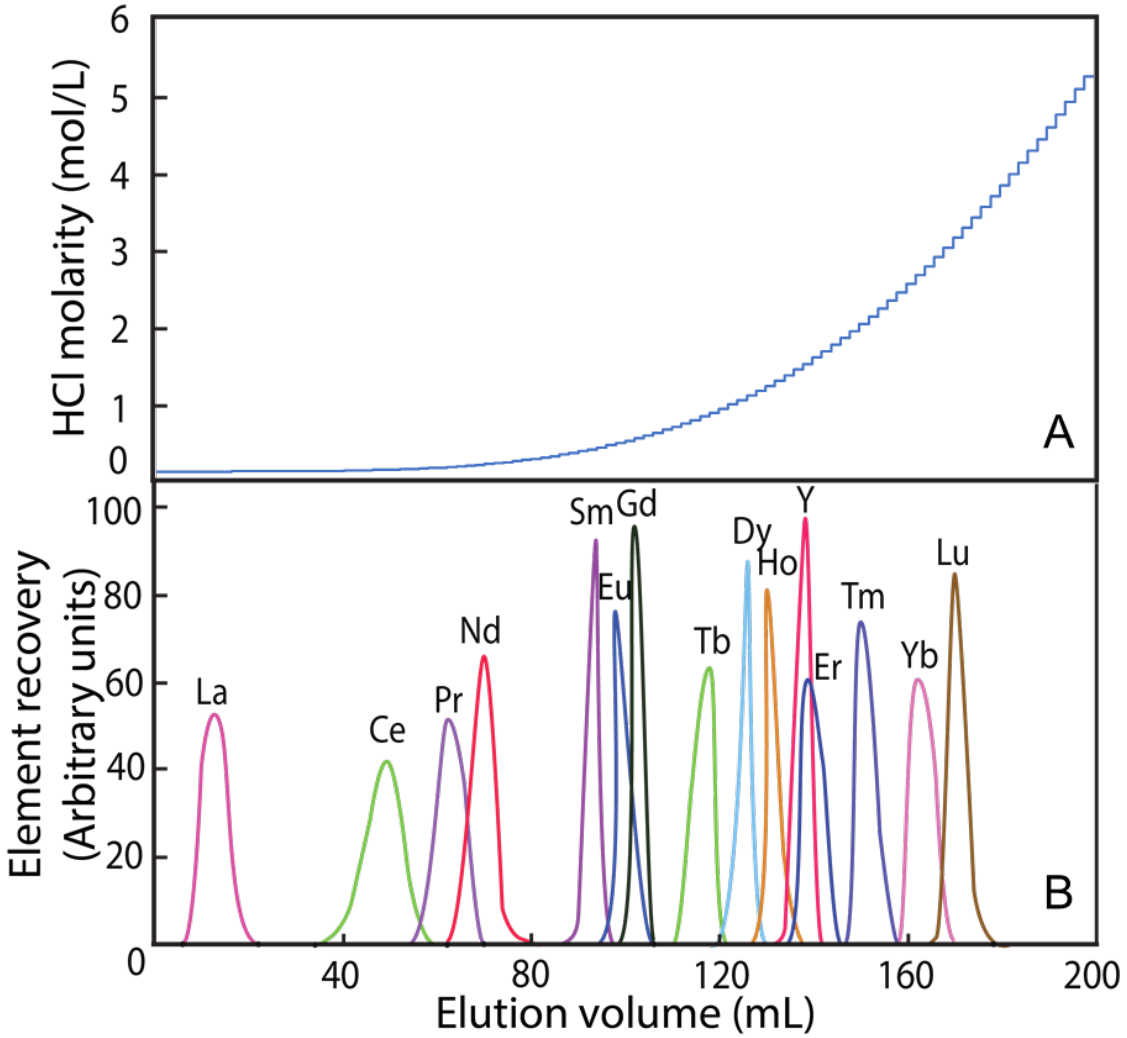

Fig. S5. FPLC elution curve of the REEs (**A**) HCl molarity of the elution solution injected in the column as a function of volume. (**B**) REE recovery as a function of elution volume. The chromatography column is 70 cm long, 1.6 mm in diameter, filled with 1.4 mL of Ln-Spec resin (*29*), and heated at 70 °C.

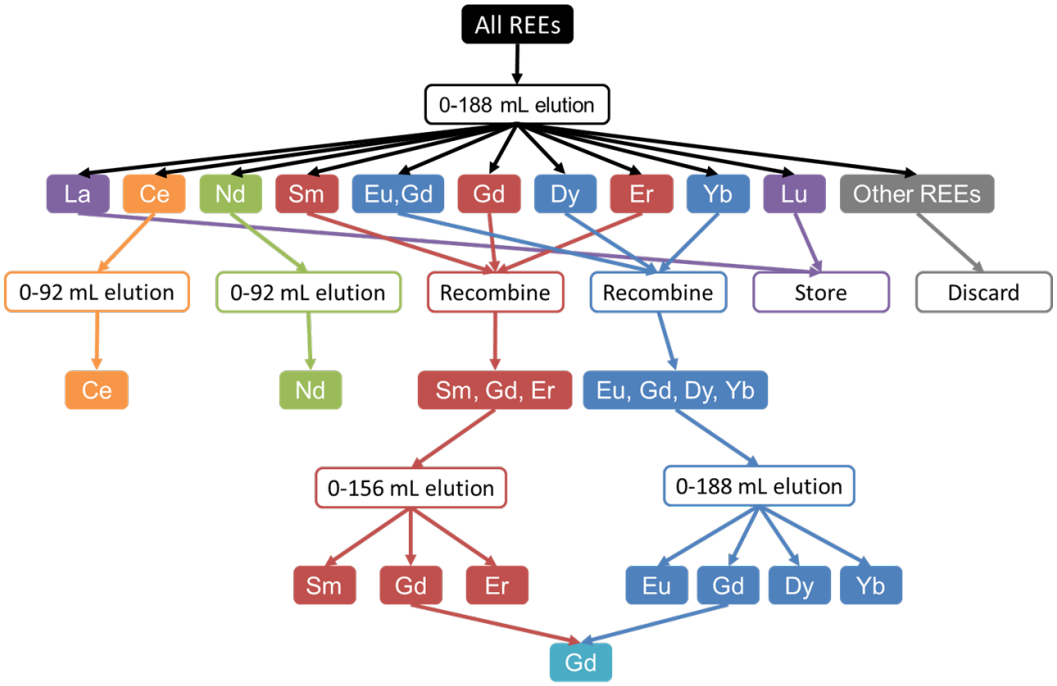

Fig. S6. Flowchart of 2-step FPLC elution of the REEs. Each elution in the flowchart uses the same gradient elution of HCl displayed in Fig. S5A but ends at different acid volume. After the first elution, REEs that are not neighbor to each other (*i.e.*, Sm/Gd/Er and Eu/Dy/Yb) are recombined and loaded onto the FPLC system (Fig. S1) for a second elution. The Eu cut from the first 0–188 mL elution contains minor Gd, which is separated from the second 0–188 mL elution and recombined with Gd cut from the 0–156 mL elution.

Table. S1. Titanium isotopic fractionation (determined by double spike) and isotopic anomalies of geostandards and CAIs

Sample	Name	ε^{46}Ti	ε^{48}Ti	ε^{50}Ti	δ^{Φ}Ti (SSB)	δ^{Φ}Ti (DS)
G3						0.21 ± 0.06
BCR2					0.01 ± 0.08	-0.01 ± 0.06
TS32		1.79 ± 0.06	0.45 ± 0.04	9.27 ± 0.09	0.07 ± 0.08	0.04 ± 0.06
ME-3364-22.2	FG-FT-2	1.61 ± 0.50	0.31 ± 0.30	9.76 ± 0.67	0.06 ± 0.12	0.30 ± 0.06
ME-3364-25.2	FG-FT-3	1.76 ± 0.36	0.48 ± 0.23	10.01 ± 0.32	0.24 ± 0.04	0.64 ± 0.06
ME-2639-16.2	FG-FT-4	1.77 ± 0.12	0.42 ± 0.07	9.35 ± 0.13	1.02 ± 0.07	0.99 ± 0.06
ME-2639-49.7	FG-FT-6	2.51 ± 0.55	-0.03 ± 0.40	12.98 ± 0.42	0.57 ± 0.52	0.75 ± 0.06
ME-2639-51.1	FG-FT-7	1.55 ± 0.57	0.25 ± 0.08	6.54 ± 0.30	-0.37 ± 0.19	-0.05 ± 0.06
AL3S5	FG-FT-8	1.52 ± 0.48	-0.46 ± 0.39	8.16 ± 0.88	0.32 ± 0.28	0.69 ± 0.06
AL4S6	FG-FT-9	2.02 ± 0.09	0.12 ± 0.05	13.71 ± 0.07	0.20 ± 0.05	0.36 ± 0.06
AL8S2	FG-FT-10	2.15 ± 1.98	0.53 ± 1.05	9.54 ± 1.53	-0.36 ± 0.57	-0.19 ± 0.06
AL10S1	FG-FT-11	1.97 ± 1.98	0.64 ± 1.05	9.39 ± 1.53	-0.63 ± 0.57	-0.20 ± 0.06

εTi is normalized to $^{49}Ti/^{47}Ti = 0.74977$; isotopic anomalies and stable isotopic fractionations (relative to the OL-Ti standard) using sample-standard bracketing (SSB) are published in (*15*). Some sample names in Table 1 of (*15*) were incorrect and are corrected in the present table.

Table. S2. Cup configuration of analyzed REEs.

		Cup configurations								
		L4	L3	L2	L1	C	H1	H2	H3	H4
Ce	Main	^{131}Xe	-	^{136}Ce	^{137}Ba	^{138}Ce	^{139}La	^{140}Ce	^{142}Ce	^{145}Nd
Nd	Main	^{140}Ce	^{142}Nd	^{143}Nd	^{144}Nd	^{145}Nd	^{146}Nd	^{148}Nd	^{150}Nd	^{152}Sm
Sm	Main	^{144}Sm	^{145}Nd*	^{147}Sm	^{148}Sm	^{149}Sm	^{150}Sm	^{152}Sm	^{154}Sm	^{156}Gd*
Eu	Main	-	^{151}Eu	^{153}Eu	^{156}Dy	^{158}Dy	^{161}Dy	^{162}Dy	^{164}Dy	^{166}Er*
Gd	Main	^{150}Sm*	^{152}Gd	^{154}Gd	^{155}Gd	^{156}Gd	^{157}Gd	^{158}Gd	^{160}Gd	^{162}Dy*
Dy	Main	^{156}Dy*	^{157}Gd*	^{158}Dy	^{160}Dy	^{161}Dy	^{162}Dy	^{163}Dy	^{164}Dy	-
	Sub	-	-	-	-	^{163}Dy^{n}	^{164}Dy	-	^{166}Er	-
Yb	Main	^{168}Yb	^{170}Yb	^{171}Yb	^{172}Yb	^{173}Yb	^{174}Yb	^{175}Lu*	^{176}Yb	^{180}Hf*
	Sub	^{166}Er	-	^{169}Tm	-	^{171}Yb	^{172}Yb	^{173}Yb^{n}	-	^{178}Hf

Faraday cups with * are connected to 10^{12} Ω amplifiers while the ones unlabeled are connected to 10^{11} Ω amplifiers.

Faraday cups with n are used to normalize the signals of subconfigurations to the main configurations.

REFERENCES AND NOTES

1. A. G. W. Cameron, The formation of the sun and planets. *Icarus* **1**, 13–69 (1962).
2. L. Grossman, Condensation in the primitive solar nebula. *Geochim. Cosmochim. Acta* **36**, 597–619 (1972).
3. S. Yoneda, L. Grossman, Condensation of CaO-MgO-Al_2O_3-SiO_2 liquids from cosmic gases. *Geochim. Cosmochim. Acta* **59**, 3413–3444 (1995).
4. T. Tanaka, A. Masuda, Rare-earth elements in matrix, inclusions, and chondrules of the Allende meteorite. *Icarus* **19**, 523–530 (1973).
5. B. Mason, S. R. Taylor, Inclusions in the Allende meteorite. *Smithson. Contrib. Earth Sci.* (1982).
6. T. R. Ireland, B. Fegley Jr., The solar system's earliest chemistry: Systematics of refractory inclusions. *Int. Geol. Rev.* **42**, 865–894 (2000).
7. N. Dauphas, A. Pourmand, Thulium anomalies and rare earth element patterns in meteorites and Earth: Nebular fractionation and the nugget effect. *Geochim. Cosmochim. Acta* **163**, 234–261 (2015).
8. J.-A. Barrat, N. Dauphas, P. Gillet, C. Bollinger, J. Etoubleau, A. Bischoff, A. Yamaguchi, Evidence from Tm anomalies for non-CI refractory lithophile element proportions in terrestrial planets and achondrites. *Geochim. Cosmochim. Acta* **176**, 1–17 (2016).
9. F. M. Richter, A. M. Davis, D. S. Ebel, A. Hashimoto, Elemental and isotopic fractionation of Type B calcium-, aluminum-rich inclusions: Experiments, theoretical considerations, and constraints on their thermal evolution. *Geochim. Cosmochim. Acta* **66**, 521–540 (2002).
10. A. Shahar, E. D. Young, Astrophysics of CAI formation as revealed by silicon isotope LA-MC-ICPMS of an igneous CAI. *Earth Planet. Sci. Lett.* **257**, 497–510 (2007).
11. F. M. Richter, P. E. Janney, R. A. Mendybaev, A. M. Davis, M. Wadhwa, Elemental and isotopic fractionation of type B CAI-like liquids by evaporation. *Geochim. Cosmochim. Acta* **71**, 5544–5564 (2007).
12. L. Grossman, S. B. Simon, V. K. Rai, M. H. Thiemens, I. D. Hutcheon, R. W. Williams, A. Galy, T. Ding, A. V. Fedkin, R. N. Clayton, T. K. Mayeda, Primordial compositions of refractory inclusions. *Geochim. Cosmochim. Acta* **72**, 3001–3021 (2008).
13. A. N. Krot, E. R. Scott, M. E. Zolensky, Mineralogical and chemical modification of components in CV3 chondrites: Nebular or asteroidal processing? *Meteoritics* **30**, 748–775 (1995).

14. J. I. Simon, M. K. Jordan, M. J. Tappa, E. A. Schauble, I. E. Kohl, E. D. Young, Calcium and titanium isotope fractionation in refractory inclusions: Tracers of condensation and inheritance in the early solar protoplanetary disk. *Earth Planet. Sci. Lett.* **472**, 277–288 (2017).
15. A. M. Davis, J. Zhang, N. D. Greber, J. Hu, F. L. Tissot, N. Dauphas, Titanium isotopes and rare earth patterns in CAIs: Evidence for thermal processing and gas-dust decoupling in the protoplanetary disk. *Geochim. Cosmochim. Acta* **221**, 275–295 (2018).
16. B. L. A. Charlier, F. L. H. Tissot, N. Dauphas, C. J. N. Wilson, Nucleosynthetic, radiogenic and stable strontium isotopic variations in fine-and coarse-grained refractory inclusions from Allende. *Geochim. Cosmochim. Acta* **265**, 413–430 (2019).
17. K. Lodders, Solar system abundances and condensation temperatures of the elements. *Astrophys. J.* **591**, 1220 (2003).
18. W. V. Boynton, Fractionation in the solar nebula: Condensation of yttrium and the rare earth elements. *Geochim. Cosmochim. Acta* **39**, 569–584 (1975).
19. A. M. Davis, L. Grossman, Condensation and fractionation of rare earths in the solar nebula. *Geochim. Cosmochim. Acta* **43**, 1611–1632 (1979).
20. A. S. Kornacki, B. Fegley Jr., The abundance and relative volatility of refractory trace elements in Allende Ca, Al-rich inclusions: Implications for chemical and physical processes in the solar nebula. *Earth Planet. Sci. Lett.* **79**, 217–234 (1986).
21. G. Pound, J. Hirth, Condensation and evaporation, nucleation and growth kinetics. *Prog. Mater. Sci.* **11** (1963).
22. F. M. Richter, Timescales determining the degree of kinetic isotope fractionation by evaporation and condensation. *Geochim. Cosmochim. Acta* **68**, 4971–4992 (2004).
23. A. Tsuchiyama, S. Tachibana, T. Takahashi, Evaporation of forsterite in the primordial solar nebula; rates and accompanied isotopic fractionation. *Geochim. Cosmochim. Acta* **63**, 2451–2466 (1999).
24. K. Ozawa, H. Nagahara, Chemical and isotopic fractionations by evaporation and their cosmochemical implications. *Geochim. Cosmochim. Acta* **65**, 2171–2199 (2001).
25. N. Dauphas, F. Poitrasson, C. Burkhardt, H. Kobayashi, K. Kurosawa, Planetary and meteoritic Mg/Si and δ^{30}Si variations inherited from solar nebula chemistry. *Earth Planet. Sci. Lett.* **427**, 236–248 (2015).
26. B. Bourdon, C. Fitoussi, Isotope fractionation during condensation and evaporation during planet formation processes. *ACS Earth Space Chem.* **4**, 1408–1423 (2020).

27. A. V. Fedkin, L. Grossman, F. J. Ciesla, S. B. Simon, Mineralogical and isotopic constraints on chondrule formation from shock wave thermal histories. *Geochim. Cosmochim. Acta* **87**, 81–116 (2012).
28. J. Jouzel, L. Merlivat, Deuterium and oxygen 18 in precipitation: Modeling of the isotopic effects during snow formation. *J. Geophys. Res. Atmos.* **89**, 11749–11757 (1984).
29. T. J. Ireland, F. L. H. Tissot, R. Yokochi, N. Dauphas, Teflon-HPLC: A novel chromatographic system for application to isotope geochemistry and other industries. *Chem. Geol.* **357**, 203–214 (2013).
30. N. Dauphas, F. L. Tissot, R. Yokochi, T. J. Ireland, J. Hu, U.S. Patent 9,884,266 (2018).
31. J. Jiun-San Shen, T. Lee, 138La anomaly in the early solar system. *Astrophys. J. Lett.* **596**, L109 (2003).
32. A. Pourmand, N. Dauphas, T. J. Ireland, A novel extraction chromatography and MC-ICP-MS technique for rapid analysis of REE, Sc and Y: Revising CI-chondrite and Post-Archean Australian Shale (PAAS) abundances. *Chem. Geol.* **291**, 38–54 (2012).
33. E. Albalat, P. Telouk, F. Albarède, Er and Yb isotope fractionation in planetary materials. *Earth Planet. Sci. Lett.* **355**, 39–50 (2012).
34. F. L. H. Tissot, N. Dauphas, L. Grossman, Origin of uranium isotope variations in early solar nebula condensates. *Sci. Adv.* **2**, e1501400 (2016).
35. F. Moynier, A. Bouvier, J. Blichert-Toft, P. Telouk, D. Gasperini, F. Albarede, Europium isotopic variations in Allende CAIs and the nature of mass-dependent fractionation in the solar nebula. *Geochim. Cosmochim. Acta* **70**, 4287–4294 (2006).
36. S. B. Simon, L. Grossman, A. M. Davis, Fassaite composition trends during crystallization of Allende Type B refractory inclusion melts. *Geochim. Cosmochim. Acta* **55**, 2635–2655 (1991).
37. N. Dauphas, M. Y. Hu, E. M. Baker, J. Hu, F. L. H. Tissot, E. Ercan Alp, M. Roskosz, J. Zhao, W. Bi, J. Liu, J.-F. Lin, N. X. Nie, A. Heard, SciPhon: A data analysis software for nuclear resonant inelastic X-ray scattering with applications to Fe, Kr, Sn, Eu and Dy. *J. Synchrotron Radiat.* **25**, 1581–1599 (2018).
38. S. Gabelnick, G. Reedy, M. Chasanov, Infrared spectra and structure of some matrix-isolated lanthanide and actinide oxides. *J. Chem. Phys.* **60**, 1167–1171 (1974).
39. A. Stracke, H. Palme, M. Gellissen, C. Münker, T. Kleine, K. Birbaum, D. Günther, B. Bourdon, J. Zipfel, Refractory element fractionation in the Allende meteorite: Implications for solar nebula

condensation and the chondritic composition of planetary bodies. *Geochim. Cosmochim. Acta* **85**, 114–141 (2012).

40. G. J. MacPherson, A. M. Davis, Refractory inclusions in the prototypical CM chondrite, Mighei. *Geochim. Cosmochim. Acta* **58**, 5599–5625 (1994).
41. H. Palme, F. Wlotzka, K. Nagel, A. El Goresy, An ultra-refractory inclusion from the Ornans carbonaceous chondrite. *Earth Planet. Sci. Lett.* **61**, 1–12 (1982).
42. S. B. Simon, A. M. Davis, L. Grossman, A unique ultrarefractory inclusion from the Murchison meteorite. *Meteorit. Planet. Sci.* **31**, 106–115 (1996).
43. M. Audard, P. Abrahám, M. M. Dunham, J. D. Green, N. Grosso, K. Hamaguchi, J. H. Kastner, A. Kóspál, G. Lodato, M. M. Romanova, Episodic accretion in young stars. *Protostars Planets VI* **387** (2014).
44. G. Herbig, EX Lupi: History and spectroscopy. *Astron. J.* **133**, 2679 (2007).
45. L. Hartmann, S. J. Kenyon, The FU orionis phenomenon. *Annu. Rev. Astron. Astrophys.* **34**, 207–240 (1996).
46. A. P. Boss, C. M. D. Alexander, M. Podolak, Cosmochemical consequences of particle trajectories during FU Orionis outbursts by the early Sun. *Earth Planet. Sci. Lett*. **345**, 18–26 (2012).
47. A. P. Boss, C. M. D. Alexander, M. Podolak, Evolution of CAI-sized Particles during FU Orionis Outbursts. I. Particle Trajectories in Protoplanetary Disks with Beta Cooling. *The Astrophysical Journal* **901**, 81 (2020).
48. P. Ábrahám, A. Juhász, C. P. Dullemond, Á. Kóspál, R. van Boekel, J. Bouwman, T. Henning, A. Moór, L. Mosoni, A. Sicilia-Aguilar, N. Sipos, Episodic formation of cometary material in the outburst of a young Sun-like star. *Nature* **459**, 224–226 (2009).
49. K. D. McKeegan, J. Aléon, J. Bradley, D. Brownlee, H. Busemann, A. Butterworth, M. Chaussidon, S. Fallon, C. Floss, J. Gilmour, M. Gounelle, G. Graham, Y. Guan, P. R. Heck, P. Hoppe, I. D. Hutcheon, J. Huth, H. Ishii, M. Ito, S. B. Jacobsen, A. Kearsley, L. A. Leshin, M.-C. Liu, I. Lyon, K. Marhas, B. Marty, G. Matrajt, A. Meibom, S. Messenger, S. Mostefaoui, S. Mukhopadhyay, K. Nakamura-Messenger, L. Nittler, R. Palma, R. O. Pepin, D. A. Papanastassiou, F. Robert, D. Schlutter, C. J. Snead, F. J. Stadermann, R. Stroud, P. Tsou, A. Westphal, E. D. Young, K. Ziegler, L. Zimmermann, E. Zinner, Isotopic compositions of cometary matter returned by Stardust. *Science* **314**, 1724–1728 (2006).

50. C. M. Lisse, J. Van Cleve, A. C. Adams, M. F. A'Hearn, Y. R. Fernández, T. L. Farnham, L. Armus, C. J. Grillmair, J. Ingalls, M. J. S. Belton, O. Groussin, L. A. Mc Fadden, K. J. Meech, P. H. Schultz, B. C. Clark, L. M. Feaga, J. M. Sunshine, Spitzer spectral observations of the Deep Impact ejecta. *Science* **313**, 635–640 (2006).
51. D. Brownlee, P. Tsou, J. Aléon, C. M. O'D. Alexander, T. Araki, S. Bajt, G. A. Baratta, R. Bastien, P. Bland, P. Bleuet, J. Borg, J. P. Bradley, A. Brearley, F. Brenker, S. Brennan, J. C. Bridges, N. D. Browning, J. R. Brucato, E. Bullock, M. J. Burchell, H. Busemann, A. Butterworth, M. Chaussidon, A. Cheuvront, M. Chi, M. J. Cintala, B. C. Clark, S. J. Clemett, G. Cody, L. Colangeli, G. Cooper, P. Cordier, C. Daghlian, Z. Dai, L. D'Hendecourt, Z. Djouadi, G. Dominguez, T. Duxbury, J. P. Dworkin, D. S. Ebel, T. E. Economou, S. Fakra, S. A. J. Fairey, S. Fallon, G. Ferrini, T. Ferroir, H. Fleckenstein, C. Floss, G. Flynn, I. A. Franchi, M. Fries, Z. Gainsforth, J.-P. Gallien, M. Genge, M. K. Gilles, P. Gillet, J. Gilmour, D. P. Glavin, M. Gounelle, M. M. Grady, G. A. Graham, P. G. Grant, S. F. Green, F. Grossemy, L. Grossman, J. N. Grossman, Y. Guan, K. Hagiya, R. Harvey, P. Heck, G. F. Herzog, P. Hoppe, F. Hörz, J. Huth, I. D. Hutcheon, K. Ignatyev, H. Ishii, M. Ito, D. Jacob, C. Jacobsen, S. Jacobsen, S. Jones, D. Joswiak, A. Jurewicz, A. T. Kearsley, L. P. Keller, H. Khodja, A. L. D. Kilcoyne, J. Kissel, A. Krot, F. Langenhorst, A. Lanzirotti, L. Le, L. A. Leshin, J. Leitner, L. Lemelle, H. Leroux, M.-C. Liu, K. Luening, I. Lyon, G. M. Pherson, M. A. Marcus, K. Marhas, B. Marty, G. Matrajt, K. M. Keegan, A. Meibom, V. Mennella, K. Messenger, S. Messenger, T. Mikouchi, S. Mostefaoui, T. Nakamura, T. Nakano, M. Newville, L. R. Nittler, I. Ohnishi, K. Ohsumi, K. Okudaira, D. A. Papanastassiou, R. Palma, M. E. Palumbo, R. O. Pepin, D. Perkins, M. Perronnet, P. Pianetta, W. Rao, F. J. M. Rietmeijer, F. Robert, D. Rost, A. Rotundi, R. Ryan, S. A. Sandford, C. S. Schwandt, T. H. See, D. Schlutter, J. Sheffield-Parker, A. Simionovici, S. Simon, I. Sitnitsky, C. J. Snead, M. K. Spencer, F. J. Stadermann, A. Steele, T. Stephan, R. Stroud, J. Susini, S. R. Sutton, Y. Suzuki, M. Taheri, S. Taylor, N. Teslich, K. Tomeoka, N. Tomioka, A. Toppani, J. M. Trigo-Rodríguez, D. Troadec, A. Tsuchiyama, A. J. Tuzzolino, T. Tyliszczak, K. Uesugi, M. Velbel, J. Vellenga, E. Vicenzi, L. Vincze, J. Warren, I. Weber, M. Weisberg, A. J. Westphal, S. Wirick, D. Wooden, B. Wopenka, P. Wozniakiewicz, I. Wright, H. Yabuta, H. Yano, E. D. Young, R. N. Zare, T. Zega, K. Ziegler, L. Zimmerman, E. Zinner, M. Zolensky, Comet 81P/Wild 2 under a microscope. *Science* **314**, 1711–1716 (2006).
52. M. E. Zolensky, T. J. Zega, H. Yano, S. Wirick, A. J. Westphal, M. K. Weisberg, I. Weber, J. L. Warren, M. A. Velbel, A. Tsuchiyama, P. Tsou, A. Toppani, N. Tomioka, K. Tomeoka, N. Teslich,

M. Taheri, J. Susini, R. Stroud, T. Stephan, F. J. Stadermann, C. J. Snead, S. B. Simon, A. Simionovici, T. H. See, F. Robert, F. J. M. Rietmeijer, W. Rao, M. C. Perronnet, D. A. Papanastassiou, K. Okudaira, K. Ohsumi, I. Ohnishi, K. Nakamura-Messenger, T. Nakamura, S. Mostefaoui, T. Mikouchi, A. Meibom, G. Matrajt, M. A. Marcus, H. Leroux, L. Lemelle, L. Le, A. Lanzirotti, F. Langenhorst, A. N. Krot, L. P. Keller, A. T. Kearsley, D. Joswiak, D. Jacob, H. Ishii, R. Harvey, K. Hagiya, L. Grossman, J. N. Grossman, G. A. Graham, M. Gounelle, P. Gillet, M. J. Genge, G. Flynn, T. Ferroir, S. Fallon, D. S. Ebel, Z. R. Dai, P. Cordier, B. Clark, M. Chi, A. L. Butterworth, D. E. Brownlee, J. C. Bridges, S. Brennan, A. Brearley, J. P. Bradley, P. Bleuet, P. A. Bland, R. Bastien, Mineralogy and petrology of comet 81P/Wild 2 nucleus samples. *Science* **314**, 1735–1739 (2006).

53. S. Simon, A. Davis, L. Grossman, Origin of compact type A refractory inclusions from CV3 carbonaceous chondrites. *Geochim. Cosmochim. Acta* **63**, 1233–1248 (1999).
54. Q. R. Shollenberger, J. Render, G. A. Brennecka, Er, Yb, and Hf isotopic compositions of refractory inclusions: An integrated isotopic fingerprint of the solar system's earliest reservoir. *Earth Planet. Sci. Lett.* **495**, 12–23 (2018).
55. N. D. Greber, N. Dauphas, I. S. Puchtel, B. A. Hofmann, N. T. Arndt, Titanium stable isotopic variations in chondrites, achondrites and lunar rocks. *Geochim. Cosmochim. Acta* **213**, 534–552 (2017).
56. J. Y. Hu, N. Dauphas, Double-spike data reduction in the presence of isotopic anomalies. *J. Anal. At. Spectrom.* **32**, 2024–2033 (2017).
57. M.-A. Millet, N. Dauphas, Ultra-precise titanium stable isotope measurements by double-spike high resolution MC-ICP-MS. *J. Anal. At. Spectrom.* **29**, 1444–1458 (2014).
58. T. R. Ireland, Correlated morphological, chemical, and isotopic characteristics of hibonites from the Murchison carbonaceous chondrite. *Geochim. Cosmochim. Acta* **52**, 2827–2839 (1988).
59. G. A. Brennecka, S. Weyer, M. Wadhwa, P. E. Janney, J. Zipfel, A. D. Anbar, 238U/235U variations in meteorites: Extant 247Cm and implications for Pb-Pb dating. *Science* **327**, 449–451 (2010).
60. H. Tang, M.-C. Liu, K. D. McKeegan, F. L. Tissot, N. Dauphas, In situ isotopic studies of the U-depleted Allende CAI Curious Marie: Pre-accretionary alteration and the co-existence of 26Al and 36Cl in the early solar nebula. *Geochim. Cosmochim. Acta* **207**, 1–18 (2017).